



This is a repository copy of *Unlocking Galactic Wolf-Rayet stars with Gaia DR2 I: Distances and absolute magnitudes*.

White Rose Research Online URL for this paper:
<https://eprints.whiterose.ac.uk/156335/>

Version: Published Version

Article:

Rate, G. and Crowther, P.A. (2020) Unlocking Galactic Wolf-Rayet stars with Gaia DR2 I: Distances and absolute magnitudes. *Monthly Notices of the Royal Astronomical Society*, 493 (1). pp. 1512-1529. ISSN 0035-8711

<https://doi.org/10.1093/mnras/stz3614>

This article has been accepted for publication in *Monthly Notices of the Royal Astronomical Society* ©: 2020 The Author(s) Published by Oxford University Press on behalf of the Royal Astronomical Society. All rights reserved.

Reuse

Items deposited in White Rose Research Online are protected by copyright, with all rights reserved unless indicated otherwise. They may be downloaded and/or printed for private study, or other acts as permitted by national copyright laws. The publisher or other rights holders may allow further reproduction and re-use of the full text version. This is indicated by the licence information on the White Rose Research Online record for the item.

Takedown

If you consider content in White Rose Research Online to be in breach of UK law, please notify us by emailing eprints@whiterose.ac.uk including the URL of the record and the reason for the withdrawal request.



eprints@whiterose.ac.uk
<https://eprints.whiterose.ac.uk/>

Unlocking Galactic Wolf-Rayet stars with *Gaia* DR2 I: Distances and Absolute Magnitudes

Gemma Rate,^{*} Paul A. Crowther

Department of Physics and Astronomy, University of Sheffield, Sheffield, S3 7RH, UK

Accepted XXX. Received YYY; in original form ZZZ

ABSTRACT

We obtain distances to 383 Galactic Wolf-Rayet (WR) stars from *Gaia* DR2 parallaxes and Bayesian methods, with a prior based on HII regions and dust extinction. Distances agree with those from Bailer-Jones et al. for stars up to 2 kpc from the Sun, though deviate thereafter due to differing priors, leading to modest reductions in luminosities for recent WR spectroscopic results. We calculate visual and K-band absolute magnitudes, accounting for dust extinction contributions and binarity, and identify 188 stars with reliable absolute magnitudes. For WR and O stars within 2 kpc, we find a WR/O ratio of 0.1. The distances are used to generate absolute magnitude calibrations and obtain the *Gaia* colour magnitude diagram for WR stars. Average v^{WR} -band absolute magnitudes for WN stars range from -3.6 mag (WN3–4) to -7.0 mag (WN8–9ha), and -3.1 (WO2–4) to -4.6 mag (WC9), with standard deviations of ~ 0.6 mag. Using HII region scale heights, we identify 31 WR stars at large (3σ , $|z| \geq 156$ pc) distances from the mid-plane as potential runaways accounting for the Galactic warp, of which only 4 involve WN8–9 stars, contrary to previous claims.

Key words: stars: Wolf-Rayet – stars: massive – stars: distances – Galaxy: disc

1 INTRODUCTION

Wolf-Rayet (WR) stars are the final stages of evolution for massive O stars ($>25 M_{\odot}$, Crowther 2007). With extremely fast and dense stellar winds, they play an important role in helping to ionize HII regions and disperse natal gas left over from the star formation process. This feedback may drive and quench star formation. Additionally, WR stars are potential progenitors of long Gamma Ray Bursts (Leloudas et al. 2010) and stripped envelope supernovae, although some may collapse directly to black holes (Georgy et al. 2009).

The later stages of massive star evolution depend heavily on parameters such as initial mass and metallicity, which influence mass loss rates (Meynet & Maeder 2005). Such dependencies make modelling massive star evolution challenging. The accuracy of evolutionary models can be tested with observations, which in turn depend on reliable distances. Inaccurate distances can thus lead to an incorrect understanding of massive star evolution.

The Milky Way contains a rich population of WR stars, whose total has been estimated at 1200 ± 200 (Rosslowe & Crowther 2015b). Over half have been detected thus far¹. Of those, approximately a third have

been discovered via IR surveys (e.g. Crowther et al. 2006, Hadfield et al. 2007, Shara et al. 2009), whilst the rest are optically visible. Until now, distances to WR stars have relied upon the small subset of the population, which are thought to be members of clusters or associations (e.g. Lundström & Stenholm 1984). These stars, along with the WR population of the Magellanic Clouds (e.g. Smith 1968 and Vacca & Torres-Dodgen 1990), have been used to calculate absolute magnitude calibrations (e.g. van der Hucht 2001, Rosslowe & Crowther 2015a). The calibrations were then applied to estimate distances to field stars. As there is some variation in absolute magnitudes within spectral subtypes, the resulting distances had large uncertainties (50% according to van der Hucht 2001).

Binarity is a key additional piece of the evolutionary puzzle for massive stars. Mason et al. (2009) estimates that 40–70% of all massive stars are in binaries. Additionally, Sana et al. (2012) suggests that 70% of O stars will undergo interaction during their lifetimes. WR stars may form via Roche Lobe overflow (Kippenhahn & Weigert 1967) at the upper end of the stripped star regime (Götberg et al. 2018) and may be responsible for the high rate of observed Ibc supernovae, relative to the number of massive stars (Eldridge et al. 2013, Smith et al. 2011).

Binaries therefore have a major influence on the evolutionary trajectory of massive stars. Studying the fractions of runaways can provide an insight into how massive binaries interact and verify models involving binary physics. Here,

^{*} garate1@sheffield.ac.uk

¹ <http://pacrowther.staff.shef.ac.uk/WRcat/index.php>, v1.21

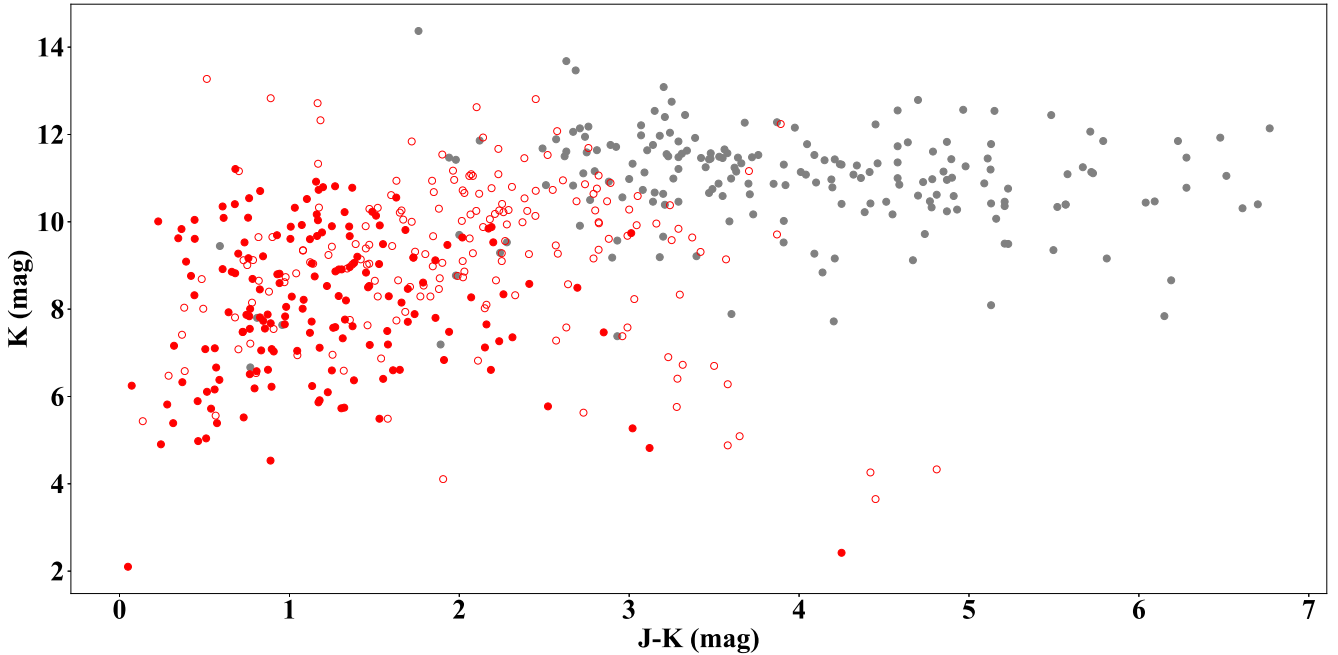


Figure 1. Plot showing the colour magnitude diagram of Galactic WR stars from the catalogue detected by *Gaia* (red) and WR stars only observed at IR wavelengths (grey). Stars not observed by *Gaia* have larger (>3) J-K colours, indicating significant extinction. Filled red circles are stars with the most reliable distances, these are limited to bright sources ($K < 12$) with $J-K < 3$.

again, accurate distances are essential to determine how far a WR star has travelled over its lifetime.

The second *Gaia* data release (Gaia Collaboration et al. 2018a, Gaia Collaboration et al. 2016, hereafter referred to as DR2) offers parallaxes, proper motions and positions for over a billion stars in the Galaxy. A large fraction of the Galactic WR population have been detected in the *Gaia* G band, (330-1050nm) and so *Gaia* increases the number of WR with trigonometric parallaxes from just one (WR11 in Hipparcos, van Leeuwen 2007) to almost 400.

In this work (Paper I) we present distances obtained using *Gaia* data and discuss the resulting new insights into Wolf-Rayet absolute magnitudes, runaways and physical parameters. In Section 2, we determine the most likely distances for Galactic WR stars using a Bayesian method and in Section 3, validate these using absolute magnitudes. We compare the new *Gaia* distances to previous values in Section 4. Distances from the Galactic midplane are discussed in section 5 and used to identify potential runaways. Finally, we conclude with an overview and anticipate potential improvements from later *Gaia* data releases.

In Paper II (Rate, Crowther & Parker, in prep), we will use these new distances and other *Gaia* DR2 results to reevaluate WR membership of clusters and associations, and discuss the implications of the results on our understanding of massive star origins and evolution. Future studies will use our distances and extinctions to calculate updated WR line luminosity calibrations for application to unresolved extragalactic WR populations.

2 DISTANCE DETERMINATION METHODS

2.1 *Gaia* DR2 catalogue

The parallax and errors used to calculate distances were taken from the *Gaia* DR2 catalogue (Gaia Collaboration et al. 2018a). The calculation also made use of *G* band magnitudes, astrometric excess noise (to identify potentially spurious results) and *Gaia* RA and Declination coordinates.

A python `ASTROQUERY` (Astropy Collaboration et al. 2013, Astropy Collaboration et al. 2018) script downloaded data from the *Gaia* archive (Salgado et al. 2017) using the ADQL query in Appendix A of the online material. The script searched for stars which were within $1''$ of the quoted WR coordinates. Almost all known WR stars are isolated enough for this constraint to be sufficient. The majority (370) of 415 successful search coordinates came from van der Hucht (2001). However, 45 coordinates from the catalogue did not lead to correct *Gaia* detections. In these instances, coordinates from SIMBAD were used instead (Wenger et al. 2000, accessed on 23/05/2018). We checked the coordinates for accuracy using images from VPHAS+ DR3 (Drew et al. 2014), IPHAS DR2 (Barentsen et al. 2014, Drew et al. 2005) and 2MASS (Skrutskie et al. 2006), to ensure they corresponded to isolated WR stars. The remaining 243 WR stars yielded no successful results with either coordinate set. Figure 1 shows most of these (>230) have $J-K > 3$ mag, indicating significant foreground dust extinction and are therefore inaccessible to *Gaia*.

383 stars (58% of the total) from the Galactic WR catalogue¹ have *Gaia* parallaxes. Of those, 305 have positive parallaxes. Figure 2 shows that both the total WR population, and the sample containing only the results with reliable dis-

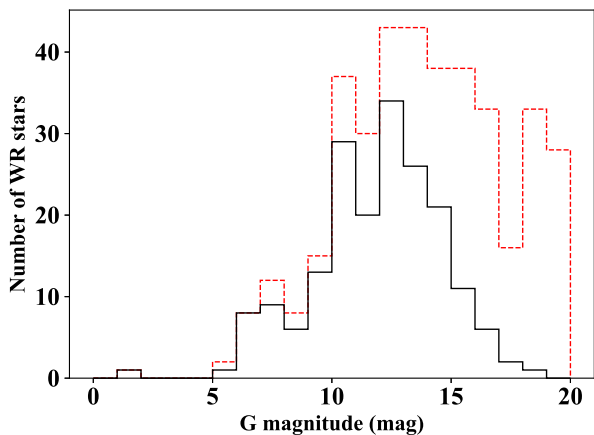


Figure 2. Histogram of G band magnitudes for Gaia DR2 detected WR stars. The solid line (black) involves 188 WR stars with reliable absolute magnitudes (Section 3) and the dashed line (red) involves the full sample of 383 WR stars.

tances, appear to be relatively complete up to $G \sim 13$ mag. However, for results with robust absolute magnitudes, the distribution falls off more quickly beyond $G \sim 13$ mag. This is because fainter magnitudes are preferentially removed due to their larger astrometric excess noise and increased incidence of negative parallaxes (which are more likely to produce unacceptable absolute magnitudes).

2.2 Bayesian methods

The conversion of *Gaia* parallaxes to distances significantly modifies the shape of the original parallax (ω) probability distribution, which means uncertainties do not transform symmetrically. This occurs unless the parallax errors (σ_ω) are very small ($\sigma_\omega/\omega < 0.1$, Bailer-Jones 2015), which is not the case for most of our DR2 sources. Additionally, many sources have negative parallaxes; a consequence of the data processing algorithm fitting noisy observations (Luri et al. 2018) and of the variation in parallax zero points (see Section 2.2.1). Obtaining the WR star distances should therefore be done carefully using Bayesian methods.

Bayesian inference is therefore the recommended way to transform parallaxes to distances (Luri et al. 2018). The end result is a probability distribution with correct uncertainties, reflecting the non symmetric transformation of parallax to distance. Bayesian methods are also capable of elegantly accounting for unphysical parallaxes and so there is no need to cut negative data from the sample (Luri et al. 2018).

The technical details of the Bayesian method used, including equations and plots of the model HII region and dust maps, are in Appendices B, C and D in the online material.

2.2.1 Likelihoods

The likelihood can be constructed by assuming the parallax distribution is Gaussian, with a mean at the parallax measured by *Gaia* and the parallax error as the standard deviation (Hogg 2018, Luri et al. 2018, Bailer-Jones 2015).

The parallaxes quoted by *Gaia* are not corrected for the

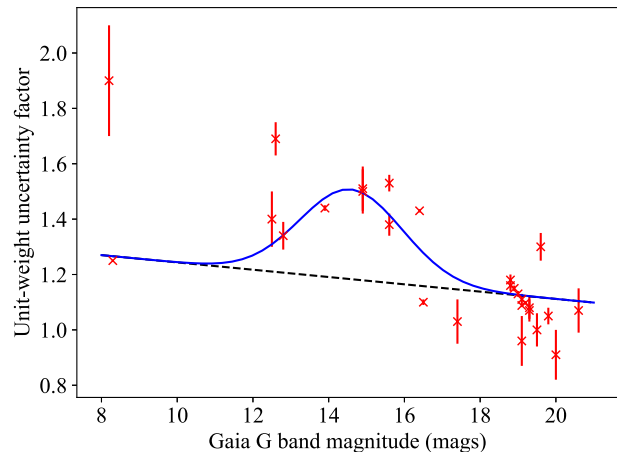


Figure 3. Weighted fit to the unit weight uncertainty factors from Arenou et al. (2018), used to increase the uncertainties σ_ω , to account for underestimation in the *Gaia* catalogue. The dotted line is the linear component of the fit, whilst the solid line is the total fit and the red crosses are the unit weight uncertainties of the external data.

global zero point. As our sample of WR stars is spread over the sky and the zero point will therefore not be dominated by regional systematics, we choose to apply this global correction to the distance calculation (Arenou et al. 2018). In light of the variation in measured zero points and the fact that Lindegren et al. (2018a) states that the zero point is likely multivariate, with no general process currently available to calculate it, we choose to use the globally measured QSO zero point of -0.029 mas (Lindegren et al. 2018b, Luri et al. 2018). One possible effect of this on the final distances is that if the full multivariate zero point could be used, some small negative parallaxes could be converted to positive values. We discuss further effects of this choice in Section 4.1.

Additionally, analysis from Arenou et al. (2018) suggests that, when compared to external data, the errors of DR2 parallaxes in the catalogue are underestimated. This is because they are consistent with the internal uncertainties, and do not account for systematics. The underestimation varies with G band magnitude and is particularly acute for results in the range $12 < G < 15$, which could be underestimated by 30-50% (Gaia Collaboration et al. 2018a).

To account for this, we calibrate the uncertainties of *Gaia* parallaxes using parallaxes from previous surveys. Arenou et al. (2018) provide in their Table 1 the unit weight error calculated using a variety of comparative surveys and the median G band of these surveys. Using this data, we present the conversion curve shown in Figure 3. This is similar to the approach of Lindegren et al. (2018a), although our model neglects the HST measurement (1.9 unit weight error at $G=8$ mag). It is possible to fit a combined Gaussian and straight line which can increase the size of the uncertainties in proportion to the G band magnitude. Details of the equation used for this fit and the impact of increasing the uncertainties on the distances are in Appendices B and E in the online material.

These increased uncertainties were applied to our WR parallaxes and lead to a likelihood that is appropriate for the WR population.

4 Rate & Crowther

2.2.2 Prior

The prior is a probability distribution of the expected distances for a given WR star. Previous work with *Gaia* (Bailer-Jones et al. 2018) has opted for a smooth, exponentially decreasing prior, with a single parameter that can be tuned based on galactic latitude and longitude. This is designed to follow the distribution of all observed stars within the Milky Way and to provide a distance derived purely from a geometric model.

Almost all WR stars are found at large (kiloparsec) distances and lie preferentially in the Galactic plane, so their observed distribution will be significantly affected by extinction. Previous priors do not properly account for this, which could be problematic for our sample.

Instead, we build a prior using HII regions and a dust model for extinction. HII regions approximate the spatial distribution of massive stars. They are independent of previous WR distribution maps, avoiding any bias from previous incorrect results and are well sampled across the galaxy (as they are detectable at a broad range of wavelengths).

To find the overall distribution, we considered HII region density along each line of sight. Figure 4 shows a mixture of Gaussians fitted to binned Galactic latitude and longitude distributions, which gave normalised numbers of HII regions at a given latitude or longitude coordinate. These were then multiplied together to get a total number density along the line of sight.

We apply a simple dust model (Rosslowe & Crowther 2015a) to account for the effects of extinction. This consists of both molecular and atomic gas, to replicate the thin and thick disks. For the Sun, we chose a distance of 8.122 kpc (Gravity Collaboration et al. 2018) to the Galactic Centre and a height of 20.8 pc (Bennett & Bovy 2019) above the plane. The resulting distribution is shown in the online supplementary material, in Appendix C.

The prior covered distances between 0 and 15 kpc, at a resolution of 1 pc. The probability is zero below 300 pc, as we do not expect to find any WR stars detected with *Gaia* closer than this distance. The final form of the prior therefore varies from Gaussian like in regions with a pronounced HII region peak or low extinction, to exponential like in regions with a less pronounced peak or high extinction.

2.2.3 Posterior

We then calculated the posterior distribution. Figure 5 shows an example of this for WR4, together with the prior and its components.

Use of the numerical dust model meant we could not differentiate the posterior and produce an analytical solution for the maximum likelihood. Instead the peak of the distribution was taken as the most likely distance. Credible intervals (similar to those used in Bailer-Jones et al. 2018) give distances which, when used as integral limits, cover 68% of the area below the curve. The one sigma errors are the differences between the peak and these distances.

2.3 Flags from *Gaia*

The validity of the distances is determined by the quality of the parallax data. A significantly negative parallax (less

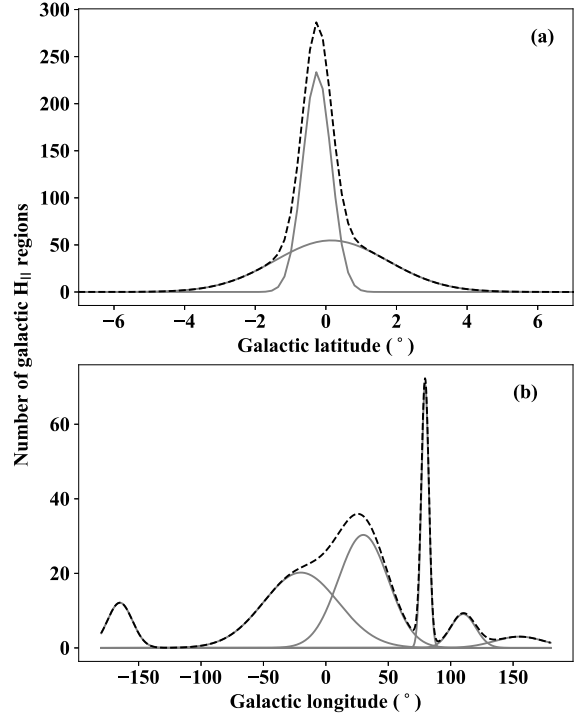


Figure 4. A mixture of Gaussians showing the number of HII regions over (a) Galactic latitude and (b) Galactic longitude, based on Figure 6 from Paladini et al. (2003) and data from Paladini et al. (2002). The solid lines are the individual Gaussians and the black dotted line is the overall fit. The peak around $l=75-90^\circ$ is the Cygnus X region.

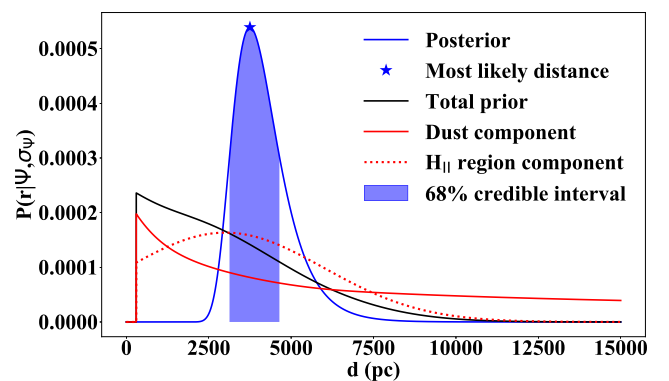


Figure 5. Posterior distribution for WR4, shown alongside the prior components and credible interval. The filled star is the most likely distance to WR4 ($3.75^{+0.89}_{-0.62}$ kpc, compared to $3.71^{+0.65}_{-0.49}$ kpc from Bailer-Jones et al. 2018).

Table 1. *Gaia* DR2 astrometric, photometric and parallax properties for 383 Galactic WR stars, including WR11 using a parallax and photometry from Hipparcos (van Leeuwen 2007). The distance for WR11 was calculated in the same manner as WR with *Gaia* results, except the adjustments to calculate ω and σ_ω were not applied. Stellar luminosities, updated from Hamann et al. (2019) and Sander et al. (2019) according to our revised distances, are restricted to sources with no error flags. The full table is available in the online supplementary material.

WR Number	Spectral Type	Alias	RA J2015	Dec J2015	$\omega \pm \sigma_\omega$ mas	d kpc	$ z $ pc	G mag	$G_{BP} - G_{RP}$ mag	Excess Noise	$\log L$ L_\odot	Flags
WR1	WN4b	HD 4004	00 43 28.39	+64 45 35.4	0.314±0.040	3.15 ^{+0.47} _{-0.36}	125 ⁺¹⁵ ₋₁₂	9.79	1.05	0.00		g
WR3	WN3ha	HD 9974	01 38 55.62	+58 09 22.6	0.342±0.051	2.90 ^{+0.52} _{-0.39}	188 ⁺³⁷ ₋₂₇	10.58	0.18	0.10	5.56	g
WR4	WC5+?	HD 16523	02 41 11.67	+56 43 49.8	0.258±0.051	3.75 ^{+0.89} _{-0.62}	174 ⁺⁴⁶ ₋₃₂	9.68	0.51	0.06	5.72	g
WR5	WC6	HD 17638	02 52 11.66	+56 56 07.1	0.334±0.042	2.97 ^{+0.43} _{-0.33}	90 ⁺¹⁶ ₋₁₂	10.06	0.94	0.00	5.53	g
WR6	WN4b	EZ CMa	06 54 13.04	-23 55 42.0	0.441±0.065	2.27 ^{+0.42} _{-0.31}	376 ⁺⁷³ ₋₅₃	6.57	0.04	0.18	5.78	g
WR7	WN4b	HD 56925	07 18 29.13	-13 13 01.5	0.221±0.051	4.23 ^{+1.08} _{-0.74}	11 ⁺² ₋₁	11.17	0.73	0.00	5.33	g
WR8	WN7o/CE	HD 62910	07 44 58.22	-31 54 29.5	0.263±0.038	3.74 ^{+0.63} _{-0.48}	226 ⁺⁴¹ ₋₃₁	9.92	0.84	0.00		g
WR9	WC5+O7	HD 63099	07 45 50.40	-34 19 48.5	0.212±0.035	4.57 ^{+0.84} _{-0.63}	256 ⁺⁷⁰ ₋₅₂	10.14	1.30	0.00		g
WR10	WN5h	HD 65865	07 59 46.24	-28 44 03.0	0.162±0.040	5.46 ^{+1.25} _{-0.91}	75 ⁺¹² ₋₉	10.94	0.60	0.09	5.78	g
WR11	WC8+O7.5III-V	γ Vel	08 09 31.96	-47 20 11.8	2.920±0.300	0.34 ^{+0.04} _{-0.03}	24 ⁺⁵ ₋₄	1.70				
WR12	WN8h	Ve5-5	08 44 47.29	-45 58 55.4	0.154±0.037	5.71 ^{+1.24} _{-0.92}	175 ⁺⁴² ₋₃₁	10.36	1.15	0.00	5.93	g

Columns are: (1) WR Name, (2) Spectral type, (3) Alternative name, (4) *Gaia* Right Ascension, (5) *Gaia* Declination, (6) Zero point corrected parallax ω and inflated error σ_ω , (7) Distance from the Sun, (8) Distance from the midplane, (9) *Gaia* G band apparent magnitude, (10) *Gaia* colour index, (11) Astrometric excess noise, (12) Stellar luminosity, (13) Error flags, a = astrometric excess noise > 1 mas; e = large parallax uncertainty $|\sigma_\omega/\omega|>1$; n = negative parallax $\omega<0$, g = good astrometry.

Table 2. Intrinsic colours of WR stars from PoWR models (Hamann & Gräfener 2004 and Todt et al. 2015 for WN, Sander et al. 2012 for WC) for $(b-v)_0^{WR}$ and monochromatic $(J-K)_0^{mono}$ and $(H-K)_0^{mono}$, and Rosslowe & Crowther (2015a) for $(J-K_s)_0$ and $(H-K_s)_0$.

WR subtype	PoWR model	$\log(T/k)$	$\log(R_t)$	$(b-v)_0^{WR}$	$(J-K_s)_0$	$(H-K_s)_0$	$(J-K)_0^{mono}$	$(H-K)_0^{mono}$
WN3-4	WNE 12-11	4.95	1.0	-0.32±0.1	-0.11±0.1	-0.03±0.1	0.24	0.16
WN4b-7b	WNE 12-18	4.95	0.3	-0.18±0.1	0.37±0.1	0.27±0.1	0.63	0.40
WN5-6	WNE 08-11	4.75	1.0	-0.28±0.1	0.18±0.1	0.16±0.1	0.30	0.20
WN7-9	WNL 06-13	4.65	0.8	-0.15±0.1	0.13±0.1	0.11±0.1	0.30	0.18
WN6ha	WNL 07-07	4.70	1.4	-0.33±0.1	-0.015±0.1	0.03±0.1	0.00	0.00
WN7ha	WNL 07-07	4.70	1.4	-0.33±0.1	-0.04±0.1	0.01±0.1	0.00	0.00
WN8-9ha	WNL 05-07	4.60	1.4	-0.32±0.1	-0.04±0.1	0.01±0.1	0.01	0.00
Of/WN	WNL 07-06	4.65	1.5	-0.34±0.1	-0.11±0.1	-0.07±0.1	-0.04	-0.03
WO2-3	WC 17-12	5.20	0.9	-0.37±0.1	0.11±0.1	0.00±0.1	0.20	0.11
WC4-7	WC 11-16	4.90	0.5	-0.20±0.2	0.62±0.1	0.58±0.2	0.54	0.33
WC8	WC 09-14	4.80	0.7	-0.37±0.1	0.43±0.1	0.38±0.1	0.38	0.21
WC9	WC 06-12	4.65	0.9	-0.32±0.1	0.23±0.1	0.26±0.1	0.12	0.09
WN/WC				-0.23±0.1	0.37±0.1	0.27±0.1		

than the zero point), will result in a smaller likelihood than a positive parallax and will increase the proportional size of the prior. Negative parallaxes can also indicate unreliable *Gaia* data. Similarly, a large error (on the scale of the data itself) will also result in a much smaller likelihood and a greater influence from the prior.

These issues mainly arise from badly fitted parallax so-

lutions, which can be identified using parameters in the *Gaia* catalogue. We chose astrometric excess noise (the observational noise which needs to be added to the data to match the solution residuals) as this identifier. Large values can indicate that a solution does not fit the data well. We chose to use this parameter, as it was the quality indicator with the clearest cut-off and acted as a good benchmark for remov-

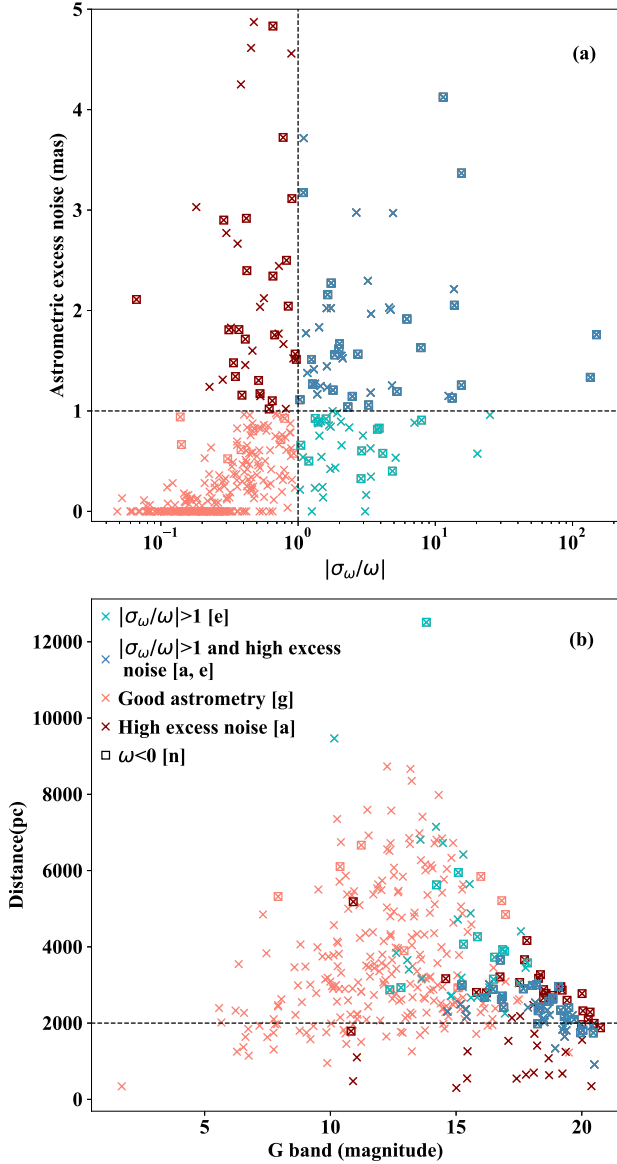


Figure 6. (a) Comparison between parallax error $|\sigma_\omega/\omega|$ and astrometric error noise (mas) for Galactic WR stars from *Gaia* DR2, for which dotted lines indicate values of unity for each parameter to highlight data quality flags a, e, g, n; (b) Comparison between G band magnitudes and inferred distances (pc) for Galactic WR stars from *Gaia* DR2, with the dotted line marking a distance of 2 kpc.

ing bad values when calculating absolute magnitudes. The excess noise can also account for modelling errors, which are not included in the observational noise. Significant astrometric excess noise is mainly applied to fainter objects, in particular those with brighter neighbours.

The *Gaia* documentation (Hambly et al. 2018) states that high excess noise will be present in early releases and suggests that users apply their own cut-offs to determine erroneous values. The ideal excess for results with distances is zero, which indicates a good fit. However, excluding an outlier with excess noise 18 mas, the average value for our

sample is 0.71 mas and the standard deviation is 0.98 mas. Therefore, we flag all results with noise above 1 mas.

Combined, our three criteria for flagging *Gaia* data quality are

$$\begin{aligned} a &= \text{astrometric_excess_noise} > 1 \\ e &= |\sigma_\omega/\omega| > 1 \\ n &= \omega < 0. \end{aligned}$$

Results without any of these issues are given the 'g' flag. These flags are applied to the distances in Table 1.

We apply the flags to the zero point corrected parallaxes and the increased errors, as these are the values are used to calculate distance. A star can be flagged if it satisfies one or more of the criteria. If all three are applied, then 37% of the WR stars with parallaxes have an a, e or n flag.

59% of the flagged results had more than one negative flag. This reflects the way such errors are intertwined, where a poor solution fit due to noisy observations can lead to a large astrometric excess noise, sizeable errors and negative parallaxes all at once.

The relations between flags are shown in Figure 6. In general, WR stars with large astrometric excess noise are supposedly located closer than 4 kpc, and in many cases closer than 2 kpc. This latter group further breaks down into brighter objects at around $G=11$ mag (WR146 and WR115) and $G=15$ mag (including WR77p) and fainter objects with $G > 17$ mag. The fainter objects may have high excess noise because of astrometric modelling difficulties, caused by issues like binarity or a badly determined spacecraft attitude during a given time interval (Hambly et al. 2018, Lindgren et al. 2018b). These problems would make it difficult for the *Gaia* AGIS algorithm to reliably extract astrometric parameters. The brighter objects may have high excess noise because of a variety of reasons, such as issues with instrument calibration (Lindgren et al. 2018b). High astrometric excess noise can also occur if the stars are in binaries (WR146) or potential binaries (WR115).

The other two flags show a less clear breakdown. Negative parallaxes can occur at all magnitudes and distances, but have non zero excess noise. Only a small fraction of results with large error ratios have zero astrometric excess noise and none at all occur below $G=12$ mag. Both flags become increasingly common beyond $G=15$ mag and only a few points beyond $G=18$ mag are not flagged. This is expected given that highly reddened objects at any distance are more difficult for *Gaia* to observe. The flags applied to the data are listed in Table 1. Any users should note that distances to these flagged stars may be suspect and should account for this in their analysis.

3 ABSOLUTE MAGNITUDES

In addition to the *Gaia* data quality flags, we checked the validity of the distance results by calculating absolute magnitudes in the v^{WR} -band (Smith 1968)², designed to avoid WR emission lines, and the K_s band. As part of this, we calculated extinction using intrinsic colours and an adopted extinction law. The result was then combined with distances and apparent magnitudes to obtain absolute magnitudes.

² A 'WR' superscript is added to distinguish the Smith v filter from the standard Johnson V-band filter

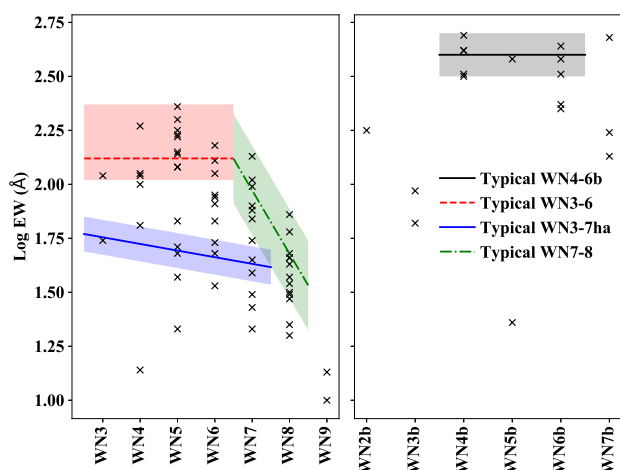


Figure 7. WN stars with HeII 4686Å equivalent widths from Conti & Massey (1989) and Smith et al. (1996). The lines show the equivalent width for a typical single WN star at each subtype. The shaded regions should contain only single stars.

3.1 Intrinsic colours for single stars

Intrinsic optical colours were taken from PoWR grids (Hamann & Gräfener 2004 and Todt et al. 2015 for WN, Sander et al. 2012 for WC), for single stars in the v^{WR} band (see Table 2). The exception is for WN/WC stars, as the value $(b-v)_0^{\text{WR}} = -0.23$ is averaged from the $E(b-v)^{\text{WR}}$ values of Sander et al. (2012) and the b^{WR} and v^{WR} apparent magnitudes of each star. Intrinsic colours for the J, H and K_s bands are taken from Rosslove & Crowther (2015a), with monochromatic near-IR PoWR synthetic colours also included.

3.2 Intrinsic colours for binary systems

16% (61 stars) of our WR sample were classified as binaries. For these systems, we calculated absolute magnitudes in the same manner as single stars, but included the companion in the intrinsic colour by measuring the dilution of the strongest optical emission lines. These are HeII 4686Å for WN stars, and CIV 5808Å and CIII 5696Å for WC stars. We fit the relation of the equivalent width to subtype for single stars (see Figs 7–8), to obtain the equivalent width of a ‘typical’ single star with a particular subtype.

For WC stars, we used CIV 5808Å to obtain the typical equivalent width of a single WR star with subtype 4, 5 or 6. In subtypes 8 and 9, the dominant line is instead CIII 5696Å. The fractions for WC7, which can contain either line, were the average dilution of the two. The fractional contribution of the WR’s visible light ($F_{C_{\text{WRv}}}$) to the binary was then found using:

$$F_{C_{\text{WRv}}} = \frac{EW_b}{EW_s} \quad (1)$$

where EW_b is the WR equivalent width for the binary and EW_s is the equivalent width for a single star. We summed the intrinsic colour of each component, weighted by contribution fraction, to obtain the colour for the system.

WR stars contribute a higher fraction of the continuum flux to the binary at near-IR wavelengths with respect to the

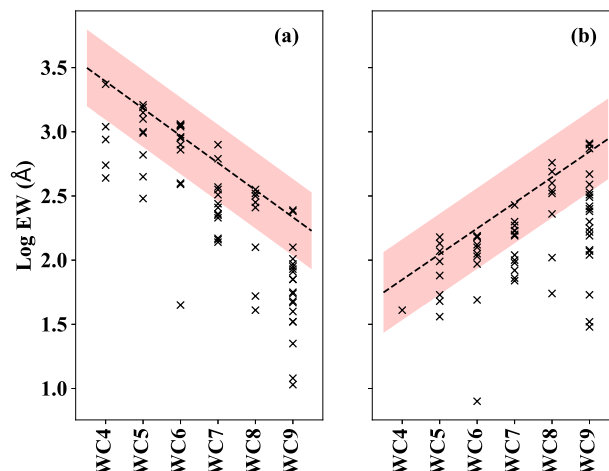


Figure 8. Equivalent widths of (a) CIV 5808Å and (b) CIII 5696Å from Torres et al. (1986), Conti & Massey (1989), Smith et al. (1990), Cohen et al. (1991), Mauerhan et al. (2009) and Zhekov et al. (2014) showing the relation between line strengths and spectral types for both single and binary stars. The dotted line shows the equivalent width for a typical single WC star at each subtype. The shaded region is the one sigma standard deviation and should contain only single stars.

Table 3. The relative continuum flux contribution of WR stars to O-type companions at near-IR wavelengths for various subtypes, adopting a Kurucz ATLAS O star model with $T_{\text{eff}} = 37500\text{K}$ and $\log g = 5$ for the companion, assuming each contribute 50% of the V-band continuum flux.

WR subtypes	F_{WR}/F_0			
	V	J	H	K
WNE-w	1	1.33	1.56	1.94
WNE-s	1	2.45	3.35	4.56
WN6ha	1	1.22	1.38	1.63
WN8	1	2.03	2.70	3.55
WN9	1	1.33	1.5	1.78
Of/WN	1	1.17	1.22	1.33
WC4-5	1	2.03	2.57	3.55
WC6-7	1	1.94	2.45	3.35
WC8	1	1.86	2.23	3.00
WC9	1	1.70	2.13	2.57

visual (see Table 3). To illustrate this, we compare template spectra from WR stars of different subtypes to an O star from a Kurucz ATLAS model ($T_{\text{eff}} = 37500\text{K}$ and $\log g = 5$). Each template spectrum is set to the same V-band continuum flux. The fraction of light contributed by the template O star at IR wavelengths can then be calculated. We use this to obtain the intrinsic colours of the binary in the same way as optical wavelength colours.

For WR11, we used the light ratio derived in De Marco et al. (2000) and for WR104, we used the ratio from Williams & van der Hucht (2000). For WR30a, we estimated the fraction of light contributed by the WR was 10%, based on the emission line strength of similar WO4 star BAT99-123 (Br93, Sand 2). For WR64-4, we used the

HeII 1.16 μ m, 1.69 μ m and 2.19 μ m IR lines to find contribution ratios, as no optical data were available. For WR35a, a reverse approach was followed based on the absolute magnitude of the system and assuming an absolute V magnitude for the O8.5V companion (from [Martins & Plez 2006](#)), to calculate the absolute magnitude of the WR component.

3.3 Optical and IR extinctions

We calculate dust extinctions using the intrinsic colours (Table 2) and apparent magnitudes in the v^{WR} band taken from the Galactic Wolf-Rayet catalogue, which was primarily compiled from [van der Hucht \(2001\)](#) and [Torres-Dodgen & Massey \(1988\)](#). J, H and K_s band magnitudes were primarily sourced from the 2MASS catalogue. The K_s band extinction, A_{K_s} , was calculated using the standard extinction law $A_{K_s} = 0.125A_v^{\text{WR}}$ (obtained from $A_{K_s} = 0.114A_v$ from [Cardelli et al. 1989](#) and $A_v^{\text{WR}} = 1.1A_v$ from [Turner 1982](#)), if values of A_v^{WR} were available. Otherwise, A_{K_s} was calculated with the relations of A_H and A_J to A_{K_s} (using parameters from [Fritz et al. 2011](#) towards the Galactic Centre and [Stead & Hoare 2009](#) elsewhere, as in [Rosslowe & Crowther 2015a](#)).

For WR25, known to have an anomalous extinction curve, we calculated A_v^{WR} using $R_v^{\text{WR}} = 6.2$ from [Crowther et al. \(1995\)](#).

Since dust extinction preferentially attenuates blue wavelengths, the *Gaia* $G_{BP} - G_{RP}$ can be used as a proxy for extinction. Some stars had unusually high K_s band extinctions (possibly due to incorrect photometry), which led to erroneous absolute magnitudes. Figure 9(a) shows the relationship between $(G_{BP} - G_{RP})$ and A_{K_s} , while Fig 9(b) compares $(G_{BP} - G_{RP})$ and A_v^{WR} . A 5σ (grey dashed lines) cutoff from the line of best fit (black solid line) was used to exclude incorrect extinctions. Some values of A_v^{WR} were also excluded for being outliers, indicating an issue either with some photometry or the $G_{BP} - G_{RP}$ magnitudes.

To obtain meaningful results at low $G_{BP} - G_{RP}$ (where we have no observations) we ensure that the extinction is zero at the intrinsic colour, $(G_{BP} - G_{RP})_0$. We obtain $(G_{BP} - G_{RP})_0$ for a generic blue energy distribution, namely a B0V spectral type, with $V - I = -0.44$ in the Johnson filter ([Ducati et al. 2001](#)). We transform this relation to the Cousins system ([Bessell 1979](#)) and finally to $(G_{BP} - G_{RP})_0 = -0.43$, using the $V - I$ to $G_{BP} - G_{RP}$ calibration in [Evans et al. \(2018\)](#).

Carrasco & Jordi (priv. comm) (using methodology from [Jordi et al. 2010](#)) provide the transformation from A_v to A_G by artificially reddening template PoWR WR spectra with different extinctions (from $A_v \sim 0.5$ to 36 mag). Synthetic photometry for the *Gaia* ([Maíz Apellániz & Weiler 2018](#)) passbands was then obtained at each A_v . This allowed for the calculation of $E(G_{BP} - G_{RP})$ and A_G . The results from Carrasco & Jordi allow us to find the intrinsic colour $(G_{BP} - G_{RP})_0$ for each WR subtype. The generic B0V model we have used to calculate $(G_{BP} - G_{RP})_0$, is within the uncertainty of the average WR value $(G_{BP} - G_{RP})_0 = -0.35 \pm 0.14$ of the subtypes in Table 4.

For the K_s band, we obtain the $G_{BP} - G_{RP}$ to A_{K_s} relationship using data with $G_{BP} - G_{RP} < 3$. This is the regime in which A_{K_s} follows the extinction law, as these stars are also observed in the v^{WR} band. At higher $G_{BP} - G_{RP}$, the calculated extinction begins to deviate from this relationship.

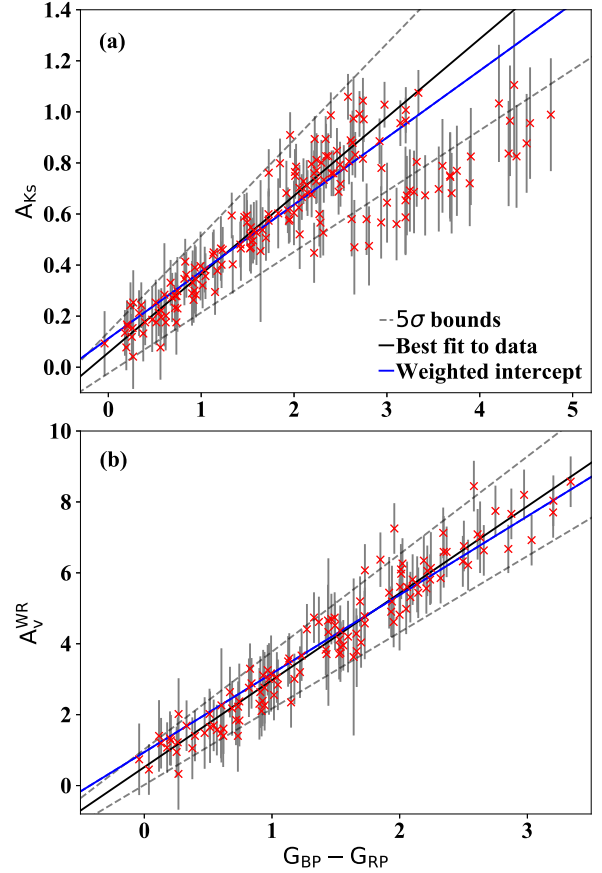


Figure 9. *Gaia* $G_{BP} - G_{RP}$ colours for Galactic WR stars compared to (a) K_s -band and (b) v^{WR} band extinctions. In (a), the solid black line presents the best fit to data with $G_{BP} - G_{RP} < 3$ while in (b), the solid line is a best fit to all data. The grey dashed lines are the 5σ bounds, based on the uncertainties of the fit parameters. The solid blue line is also the best fit to the data, but weighted so that it passes through $A_v^{\text{WR}} = 0$ at $(G_{BP} - G_{RP})_0 = -0.43$, as expected for a generic B0V star.

Table 4. Conversion equations between narrowband v^{WR} and *Gaia* G band filters for $(G_{BP} - G_{RP})_0$ of different spectral types, using results from Carrasco & Jordi.

WR class	$(G_{BP} - G_{RP})_0$	A_v^{WR} to A_G
WNE-w	-0.412	$-0.005 A_v^2 + 0.815 A_v + 0.540$
WNE-s	-0.188	$-0.005 A_v^2 + 0.803 A_v + 0.506$
WN6ha	-0.407	$-0.005 A_v^2 + 0.816 A_v + 0.531$
WN8	-0.200	$-0.004 A_v^2 + 0.802 A_v + 0.501$
WN9	-0.372	$-0.005 A_v^2 + 0.814 A_v + 0.522$
WC5	-0.659	$-0.006 A_v^2 + 0.855 A_v + 0.558$
WC7	-0.431	$-0.005 A_v^2 + 0.830 A_v + 0.573$
WC8	-0.317	$-0.005 A_v^2 + 0.808 A_v + 0.572$
WC9	-0.201	$-0.005 A_v^2 + 0.805 A_v + 0.503$
B0V SED	-0.430	$-0.005 A_v^2 + 0.816 A_v + 0.534$

Table 5. Average absolute magnitudes for Galactic Wolf-Rayet subtypes in v^{WR} and K_s band filters. In the v^{WR} band, the WC9d sample has been combined with non dusty WC9 stars.

WR subtypes	$M_{v^{\text{WR}}}$ (mag)	$N(v^{\text{WR}})$	M_{K_s} (mag)	$N(K_s)$
WN3-4	-3.6 ± 0.5	6	-3.1 ± 0.7	7
WN5-6	-4.3 ± 0.6	22	-4.0 ± 0.5	33
WN6-7ha	-6.5 ± 0.3	3	-6.2 ± 0.3	5
WN4-6b	-4.5 ± 0.6	13	-4.7 ± 0.6	15
WN7	-4.6 ± 0.6	10	-4.9 ± 0.4	15
WN8	-5.7 ± 0.6	8	-6.1 ± 0.7	13
WN8-9ha	-7.0 ± 0.4	2	-6.9 ± 0.4	2
WN9	-6.0 ± 0.8	2	-5.8 ± 0.8	6
Of/WN	-5.8 ± 0.1	2	-6.1 ± 0.1	3
WO2-4	-3.1 ± 1.4	3	-2.7 ± 1.0	4
WC4-5	-4.1 ± 0.6	11	-4.4 ± 0.4	11
WC6-7	-3.9 ± 0.4	18	-5.0 ± 0.5	23
WC8	-4.5 ± 0.9	6	-5.3 ± 0.5	7
WC9	-4.6 ± 0.4	12	-4.9 ± 0.5	9
WC9d			-6.7 ± 0.8	13

The empirical fit is shown in blue in Figure 9(a) and has the form:

$$A = X(G_{BP} - G_{RP}) + Y \quad (2)$$

where $G_{BP} - G_{RP}$ is the value from the *Gaia* catalogue, $X=0.2624$ and $Y=0.1121$. The v^{WR} band, shown in Figure 9(b), was much more closely grouped around the line of best fit, with $X=2.217$ and $Y=0.9436$. The gradient is 8.45 times the gradient for the K_s band. This is slightly larger than the $A_{K_s} = A_v/7.97$ extinction law used to calculate values of A_{K_s} with A_v . The deviation reflects the fact that some values of A_{K_s} were not calculated using that extinction law.

We can also use the synthetic photometry from Carasco & Jordi to calculate the conversion relationship from A_v^{WR} to A_G (also shown in Table 4), by converting A_v in their relationship to A_v^{WR} . This enables us to calculate the absolute *Gaia* G magnitude and present the *Gaia* colour magnitude diagram (CMD) in Figure 10, for the most reliable WR results. Fig. 10(a) presents a CMD for Galactic WR stars plus visually bright O stars from v4.1 of the Galactic O Star Catalogue (GOSC, Maíz Apellániz et al. 2013), while Fig. 10(b) compares the CMD of WR stars to 70,000 DR2 stars from *Gaia* Collaboration et al. (2018b). Two exceptionally bright stars are the extreme hypergiants He 3-519 (WR31a) and AG Car (WR31b), which exhibit very late WN characteristics at extreme visual minima (Smith et al. 1994).

3.4 Absolute magnitudes

We used the extinctions, distances and apparent magnitudes to calculate the absolute magnitudes for stars that have reliable extinctions (within the 5σ bounds of Figure 9). Repeat-

ing the calculation using a Monte Carlo selection (bootstrapping with replacement) from the distributions of the three parameters, produced a binned histogram of absolute magnitude against frequency. This acted as a proxy for the probability distribution of each absolute magnitude. A Gaussian or Weibull distribution was fit to the binned data, to find the most likely absolute magnitude and uncertainties (more details are available in Appendix F of the online material).

For binaries, the absolute magnitudes of Wolf-Rayet components were separated from the total system magnitude.

A multi step process of sigma clipping allowed us to find reliable absolute magnitudes for all WR stars. First, stars with high astrometric excess noise, or unrealistically low absolute magnitudes (≥ -1 mag) were removed from the sample. We then calculated the averages of the remaining stars in each subtype class. Stars with unusually high or low absolute magnitudes (defined as were greater than one sample standard deviation, from the mean) were then cut from the sample. This cut-off provided a good balance between excluding clearly incorrect values and including valid ones across all subtypes.

The remaining sample contained only the most reliable absolute magnitude results in each subclass and were used to calculate the averages presented in Table 5. LBVs, aside from He 3-519 (WR31a) and AG Car (WR31b), were removed due to variability. WR20-2, WR42-1, WR43-2, WR43-3 were also excluded from the averages, owing to uncertain subtypes.

We obtain K_s band results for dusty subtypes (WC8d and WC9d) by converting A_v^{WR} to A_{K_s} , using the standard extinction law. This method prevents the IR dust emission from contaminating the extinction calculation. The absolute magnitudes could then be calculated for each subtype and in each filter, with the standard deviation providing upper and lower bounds on the typical absolute magnitudes. The WC9d were combined in the v^{WR} band, but not in the K_s band, as their IR excess renders them brighter than dust free WR stars. As there were only three WC8d (WR48a, WR53 and WR113) in the final sample, these stars were grouped with the non dusty WC8 stars and only WR113 was used to calculate the final absolute K_s in Table 5. Excluding WR113 from the average, we obtain $M_{K_s} = -5.3$ mag for WC8 stars, the same result as Table 5.

In Figure 11, we present the final absolute K_s band magnitudes and uncertainties for each subtype. These are compared with corresponding values from Rosslowe & Crowther (2015a). Figure 12 shows the same distribution for the v^{WR} band, compared with van der Hucht (2001). Tables 6 and 7 show results for individual stars (the full lists are in the supplementary online material).

We additionally plot the absolute magnitudes for 116 LMC stars in Figure 12, using results from Hainich et al. (2014) for single WN and Of supergiant stars (excluding WN2b), Shenar et al. (2019) for stars in binaries, Crowther et al. (2002) for single WC stars and reddenings from Tramper et al. (2015) and v^{WR} band magnitudes from Torres-Dodgen & Massey (1988) for BAT99-123 (WO4). We adopt spectral types of LMC late WN stars from Crowther & Smith (1997) instead of Schnurr et al. (2008).

From Fig. 12, absolute v^{WR} magnitudes of LMC stars are brighter than their Galactic analogues, so it is inappropriate

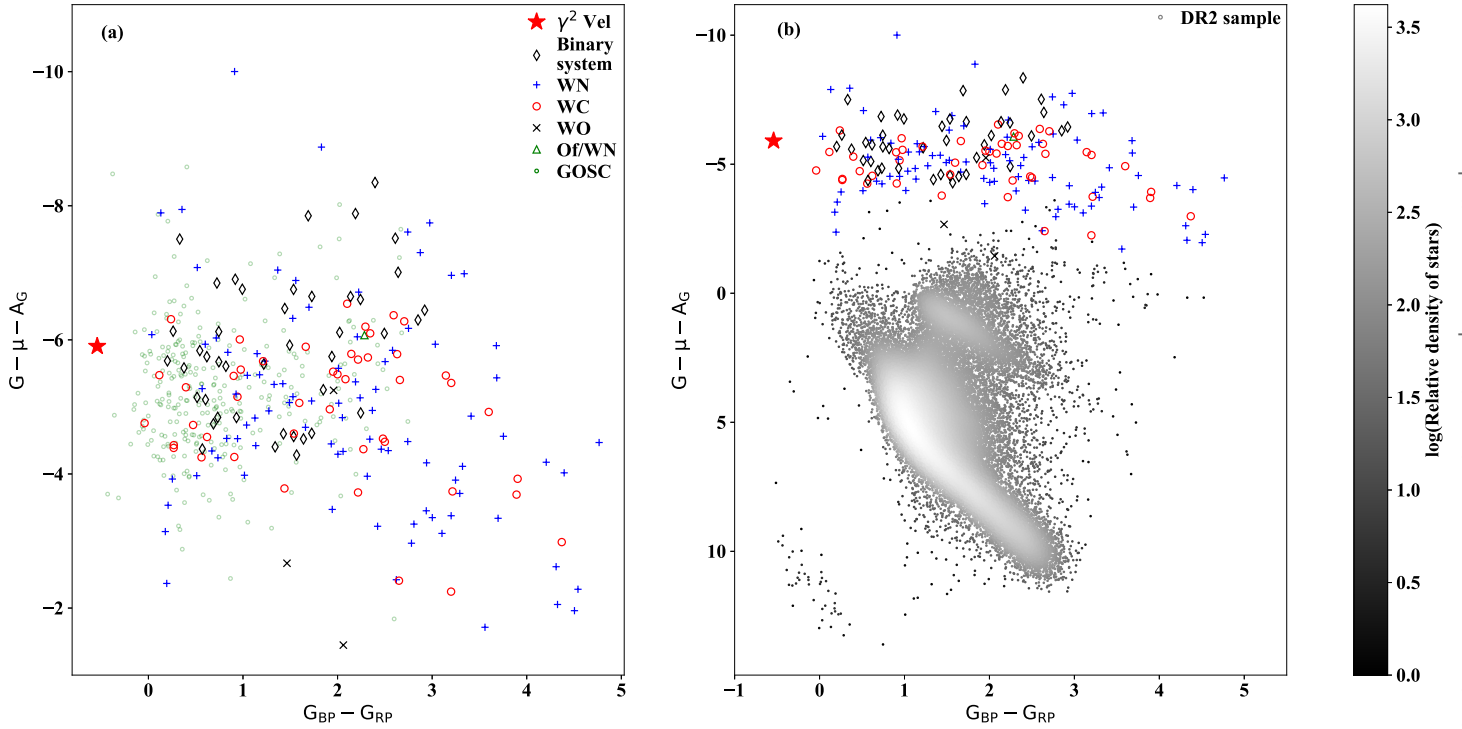


Figure 10. (a) *Gaia* DR2 colour magnitude diagram for Galactic WR stars plus O stars from GOSC (v4.1, Maíz Apellániz et al. 2013). Absolute magnitudes are calculated using our inferred distance moduli μ and A_G (converted from A_V^{WR} using the relation from Carrasco & Jordi). The red star is the WR component of γ Velorum, the only WR star with a trigonometric parallax from *Hipparcos*; (b) *Gaia* DR2 colour magnitude diagram for Galactic WR stars plus 70,000 stars from DR2, satisfying the selection criteria from section 2.1 of *Gaia* Collaboration et al. (2018b).

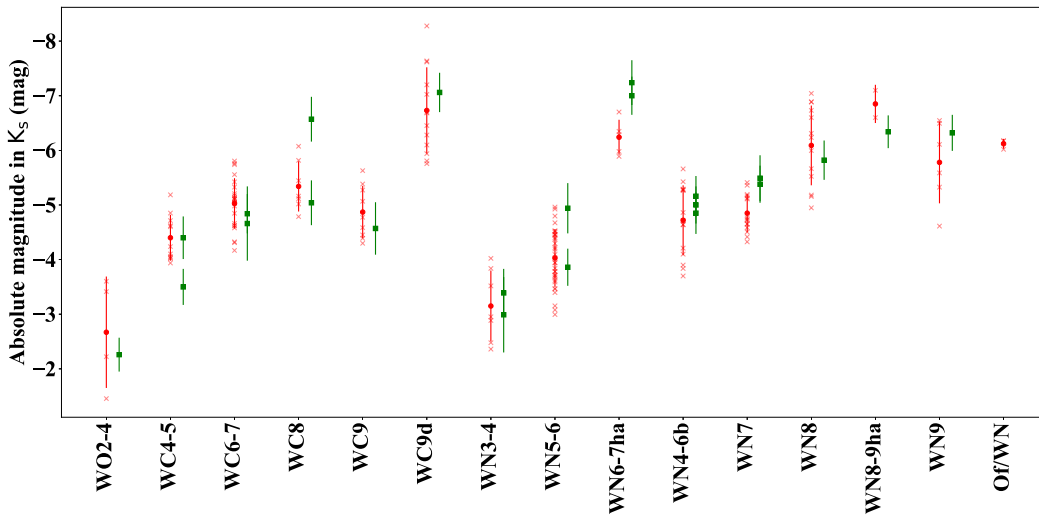


Figure 11. Absolute magnitudes in the K_s band. Red crosses are individual WR star results and the red circle is the average for each spectral subtype (with the sample standard deviation of the data as the uncertainties). Green squares are the comparative data from Rosslowe & Crowther (2015a).

to apply LMC WR absolute magnitudes to Galactic stars. LMC WN5–6 stars are particularly bright, since this sample includes the luminous H-rich main sequence WN5–6h stars whose closest Galactic analogues are WN6–7ha stars which

are amongst the visually brightest WR stars in the Milky Way.

In total, reasonable absolute magnitudes, extinctions and no *Gaia* excess noise flags, were obtained in 188 cases. Absolute magnitudes for almost all WR subtypes revealed

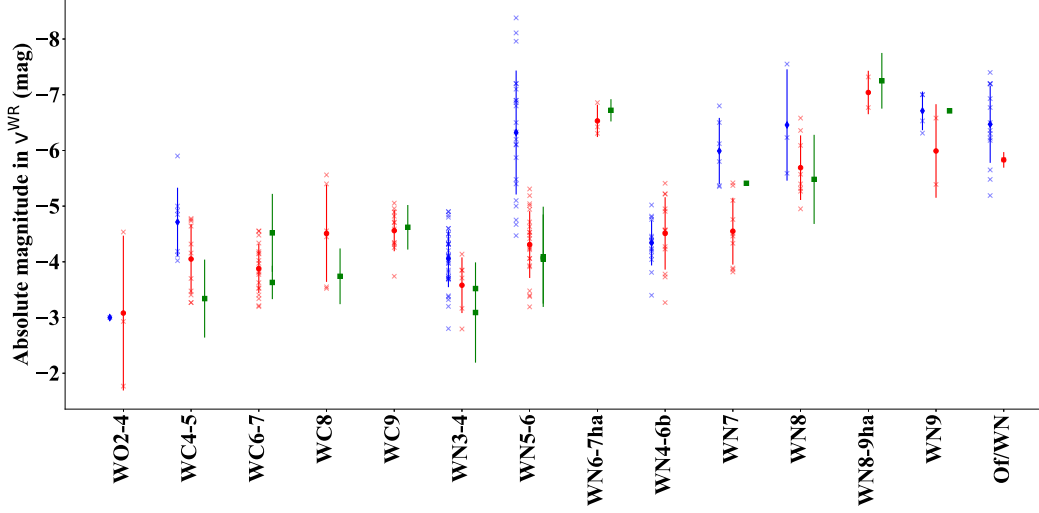


Figure 12. Absolute magnitudes in the v^{WR} band. Red crosses are individual WR star results and the red circle is the average for each spectral subtype (with the sample standard deviation of the data as the uncertainties). Green squares are the comparative data from van der Hucht (2001). Results from the LMC (Hainich et al. 2014, Shenar et al. 2019 and Crowther et al. 2002) are shown in blue, with crosses for individual stars and the diamond the average for each subtype. LMC WN5-6 stars include very luminous H-rich main sequence WN5-6h stars. Results for WO were calculated using Tramper et al. (2015) and Torres-Dodgen & Massey (1988)

Table 6. Absolute K_s -band magnitudes for Galactic WR stars. The full table is available in the online supplementary material.

WR Number	Spectral type	K_s (mag)	μ (mag)	J- K_s (mag)	H- K_s (mag)	A_{K_s} (mag)	$M_{K_s}^{\text{Sys}}$ (mag)	$F_{K_s}^{\text{WR}} / F_{K_s}^{\text{Sys}}$	$M_{K_s}^{\text{WR}}$ (mag)	Flags
WR1	WN4b	7.48	12.49	0.73	0.38	0.36±0.09			-5.4 ^{+0.2} _{-0.2}	b:
WR3	WN3ha	10.01	12.31	0.23	0.12	0.13±0.09			-2.5 ^{+0.1} _{-0.2}	b:
WR4	WC5+?	7.88	12.87	0.87	0.69	0.21±0.13			-5.3 ^{+0.4} _{-0.5}	b
WR5	WC6	7.65	12.36	0.98	0.69	0.35±0.13			-5.1 ^{+0.3} _{-0.3}	g
WR6	WN4b	5.89	11.78	0.46	0.34	0.06±0.09			-6.0 ^{+0.2} _{-0.3}	b
WR7	WN4b	9.27	13.13	0.70	0.40	0.28±0.09			-4.2 ^{+0.4} _{-0.5}	g
WR8	WN7o/CE	7.93	12.87	0.64	0.39	0.36±0.09			-5.4 ^{+0.1} _{-0.2}	b:
WR9	WC5+O7	7.54	13.3	0.91	0.57	0.52±0.09	-6.3 ^{+0.1} _{-0.1}	0.60 ± 0.24	-5.8 ^{+0.6} _{-0.5}	b
WR10	WN5h	9.61	13.69	0.44	0.28	0.28±0.20			-4.5 ^{+0.4} _{-0.4}	g

Columns: (1) WR Number, (2) Spectral type, (3) K_s apparent magnitude, (4) Distance modulus μ , (5) J- K_s colour, (6) H- K_s colour, (7) K_s band extinction A_{K_s} , (8) Absolute magnitude of binary system (including companion), (9) Fraction of light contributed to the binary system by the WR component, (10) Absolute magnitude of WR star, (11) Error flags, where $M > \text{upper}_{\text{initial}}$ or $M < \text{lower}_{\text{initial}} = \text{b}$, $M > \text{upper}_{\text{final}}$ or $M < \text{lower}_{\text{final}} = \text{b}$: (initial denotes the averages calculated before sigma clipping, final are the final absolute magnitude boundaries) and g are results with no issues.

standard deviations that overlapped with the uncertainty range of the previous results in both the v^{WR} and the K_s bands. The differences between values can be attributed to the improved distance estimates and the increased number of stars with distances. Some stars, such as WR2 (the only WN2 star, Chené et al. 2019), were not present in the *Gaia* catalogue.

There is a clear trend across both filters of increasing absolute magnitudes with increasing subtype. In both filters, WN4-6b are brighter than their weak-lined counterparts

despite their higher effective temperatures (Hamann et al. 2006). WNLha stars are known to be highly luminous, and conform to this expectation.

The spread in absolute magnitudes is similar to those previously obtained in the near-IR, but slightly larger in the v^{WR} band. Rosslowe & Crowther (2015a) quote a range of 0.3-0.6 mag, whilst the standard deviation in our K_s band results spans 0.1-1.0 mag, but is also more typically 0.3-0.6 mag. For the v^{WR} band, the standard deviations range from

Table 7. Absolute v^{WR} -band magnitudes for Galactic WR stars. The full table is available in the online supplementary material.

WR Number	Spectral type	$v^{\text{WR}} \pm 0.1$ (mag)	μ (mag)	$(b-v)^{\text{WR}}$ (mag)	A_v^{WR} (mag)	M_v^{Sys} (mag)	$F_v^{\text{WR}} / F_v^{\text{Sys}}$	M_v^{WR} (mag)	Flags
WR1	WN4b	10.51	12.49	0.51	2.84 ± 0.71			$-4.9^{+0.8}_{-0.8}$	g
WR3	WN3ha	10.70	12.31	-0.06	1.07 ± 0.71			$-2.8^{+0.8}_{-0.8}$	b:
WR4	WC5+?	10.53	12.87	0.20	1.65 ± 1.01			$-4.2^{+1.1}_{-1.1}$	g
WR5	WC6	11.02	12.36	0.47	2.76 ± 1.01			$-4.2^{+1.1}_{-1.1}$	g
WR6	WN4b	6.94	11.78	-0.07	0.45 ± 0.71			$-5.4^{+0.8}_{-0.8}$	b:
WR7	WN4b	11.75	13.13	0.36	2.22 ± 0.71			$-3.8^{+0.9}_{-0.9}$	b:
WR8	WN7o/CE	10.48	12.87	0.47	2.88 ± 0.71			$-5.4^{+0.8}_{-0.8}$	b:
WR9	WC5+O7	10.93	13.3	0.74	4.16 ± 0.72	$-6.6^{+0.8}_{-0.8}$	0.29 ± 0.12	$-5.3^{+1.4}_{-1.2}$	b
WR10	WN5h	11.08	13.69	0.22	2.26 ± 1.61			$-5.0^{+1.7}_{-1.7}$	b:

Columns: (1) WR Number, (2) Spectral type, (3) v^{WR} apparent magnitude and error, (4) Distance modulus μ , (5) $(b-v)^{\text{WR}}$ colour, (6) v^{WR} band extinction A_v , (7) Absolute magnitude of binary system (including companion), (8) Fraction of light contributed to the binary system by the WR component, (9) Absolute magnitude of WR star, (10) Error flags, where $M > \text{upper}_{\text{initial}}$ or $M < \text{lower}_{\text{initial}} = b$, $M > \text{upper}_{\text{final}}$ or $M < \text{lower}_{\text{final}} = b$: ($_{\text{initial}}$ denotes the averages calculated before sigma clipping, $_{\text{final}}$ are the final absolute magnitude boundaries) and g are results with no issues.

0.3-1.4 mag and mostly have standard deviations between 0.4-0.6 mag.

We therefore corroborate the findings of Sander et al. (2019) that WC stars of the same subtype have a broader range of absolute magnitudes than expected. We also posit this is true for WN stars (Hamann et al. 2019 also note the relations between absolute magnitude and subtype are not strict). The uncertainties show no systematic differences between WC and WN classes or regular variation across subtypes. However, particularly in the v^{WR} band, some classes suffered from very small numbers of WR stars (only 2 WN9 stars had v^{WR} band magnitudes, for instance). This increases the size of the uncertainties on the mean result.

Due to this intrinsic variation, we advise caution when using averages as absolute magnitude calibrations and recommend accounting for the large uncertainties by exploring other methods, such as a Bayesian approach with a probability distribution centred on the average magnitude. We also recommend continued use of the intrinsic colours in Table 2, rather than calculating new values using our methods and results. The large uncertainties of our absolute magnitudes, mean that propagated uncertainties of any resulting intrinsic colours are correspondingly large. These new uncertainties are far larger than the intrinsic colours from Table 2.

3.5 Sensitivity of results to adopted intrinsic colours

We test the sensitivity of the results to the intrinsic colours. For the v^{WR} band, this is straightforward in that any difference in $(b-v)_0^{\text{WR}}$ is propagated through to the extinction (so multiplied by 4.12, Turner 1982). However, within the K_s band, the combination of $(J-K_s)_0$ and $(H-K_s)_0$ complicates this somewhat and we test the effects by calculating M_{K_s} with alternative $J-K_s$ and $H-K_s$ synthetic colours. These are taken from the PoWR grids (Hamann & Gräfener 2004 and Todt et al. 2015 for WN, Sander et al. 2012 for WC), using

the same models as Table 2. Unlike the $b-v^{\text{WR}}$ colours, these are only valid at the monochromatic wavelengths and not the whole filter bands, which are affected by emission lines, especially for early-type WC stars. The difference in absolute magnitudes are between 0.05 for WN5-6 and 0.2 for WC6-7 and WN2-4 (as emission lines fall within the filter band and are not included in the monochromatic result), with most subtypes falling between 0.1 and 0.2. In all instances, this was well within the uncertainties on individual magnitudes.

3.6 Photometric Flags

In addition to the *Gaia* flag, we identify results with potentially spurious absolute magnitudes. As stars with incorrect extinctions were removed, spurious results can indicate either incorrect apparent magnitudes, or an incorrect *Gaia* parallax, whose distance generates the wrong absolute magnitude. We therefore adopt two different flags, one where the absolute magnitude is implausible and another where the absolute magnitude only just falls outside the uncertainty of the subtype average. The latter does not necessarily indicate a bad result, but these data should be treated with caution.

$$M > \text{upper}_{\text{initial}} \text{ or } M < \text{lower}_{\text{initial}} = b$$

$$M > \text{upper}_{\text{final}} \text{ or } M < \text{lower}_{\text{final}} = b:$$

where upper and lower are the upper and lower magnitude bounds of the absolute magnitude average. $_{\text{initial}}$ denotes the averages calculated before sigma clipping (Section 3), $_{\text{final}}$ are the final absolute magnitude boundaries (as in Table 5) and M is the absolute magnitude of individual WR stars. Results with a 'b' flag are highly implausible and lie well outside the range of acceptable absolute magnitudes, whilst those with a 'b:' flag are still acceptable, but fall outside the 1σ uncertainties of the results in Table 5. Again, results without any of these issues are given the 'g' flag. Results without any absolute magnitudes are flagged with 'u'. These stars were included to provide the reader with the

Table 8. WR stars within 2 kpc of the Sun, including colour excess, K-band extinction and A_{K_s} /kpc, extinction per kpc.

WR Number	Alias	Spectral type	Distance (kpc)	Flags	E(B-V)	A_{K_s}	A_{K_s} /kpc
WR11	γ Vel	WC8+O7.5III-V	$0.34^{+0.04}_{-0.03}$...	0.00 ± 0.30	0.00 ± 0.13	$0.00^{+0.38}_{-0.38}$
WR94	HD 158860	WN5o	$0.95^{+0.06}_{-0.06}$	g	1.24 ± 0.21	0.53 ± 0.09	$0.55^{+0.10}_{-0.10}$
WR90	HD 156385	WC7	$1.15^{+0.11}_{-0.09}$	g	0.10 ± 0.30	0.04 ± 0.13	$0.04^{+0.11}_{-0.04}$
WR78	HD 151932	WN7h	$1.25^{+0.15}_{-0.12}$	g	0.44 ± 0.21	0.19 ± 0.09	$0.15^{+0.07}_{-0.07}$
WR139	HD 193576	WN5o+O6III-V	$1.31^{+0.07}_{-0.06}$	g	0.81 ± 0.24	0.35 ± 0.10	$0.26^{+0.08}_{-0.08}$
WR79	HD 152270	WC7+O5-8	$1.37^{+0.12}_{-0.10}$	g	0.31 ± 0.26	0.13 ± 0.11	$0.10^{+0.08}_{-0.08}$
WR145	AS 422	WN7o/CE+?	$1.46^{+0.12}_{-0.10}$	g	2.28 ± 0.39	0.97 ± 0.16	$0.67^{+0.13}_{-0.12}$
WR110	HD 165688	WN5-6b	$1.58^{+0.15}_{-0.12}$	g	1.13 ± 0.21	0.48 ± 0.09	$0.30^{+0.06}_{-0.06}$
WR111	HD 165763	WC5	$1.63^{+0.32}_{-0.23}$	g	0.22 ± 0.30	0.09 ± 0.13	$0.06^{+0.08}_{-0.06}$
WR140	HD 193793	WC7pd+O4-5	$1.64^{+0.11}_{-0.09}$	g	0.65 ± 0.22	0.28 ± 0.09	$0.17^{+0.06}_{-0.06}$
WR142	Sand 5	WO2	$1.65^{+0.11}_{-0.09}$	g	2.13 ± 0.21	0.91 ± 0.09	$0.55^{+0.06}_{-0.06}$
WR105	NS 4	WN9h	$1.73^{+0.32}_{-0.23}$	g	2.41 ± 0.21	1.03 ± 0.09	$0.59^{+0.12}_{-0.10}$
WR134	HD 191765	WN6b	$1.75^{+0.13}_{-0.11}$	g	0.46 ± 0.21	0.20 ± 0.09	$0.11^{+0.05}_{-0.05}$
WR52	HD 115473	WC4	$1.75^{+0.16}_{-0.13}$	g	0.59 ± 0.30	0.25 ± 0.13	$0.14^{+0.07}_{-0.07}$
WR144	HM19-1	WC4	$1.75^{+0.24}_{-0.19}$	g		0.47 ± 0.19	$0.27^{+0.11}_{-0.11}$
WR93	HD 157504	WC7+O7-9	$1.76^{+0.19}_{-0.15}$	g	1.67 ± 0.23	0.71 ± 0.10	$0.40^{+0.07}_{-0.07}$
WR142-1	HBHalpha 4203-27	WN6o	$1.77^{+0.23}_{-0.18}$	g		0.69 ± 0.16	$0.39^{+0.10}_{-0.10}$
WR113	HD 168206	WC8d+O8-9IV	$1.80^{+0.24}_{-0.19}$	g	0.94 ± 0.21	0.40 ± 0.09	$0.22^{+0.06}_{-0.06}$
WR142a	PCG02 1	WC8	$1.81^{+0.61}_{-0.37}$	g		0.83 ± 0.19	$0.46^{+0.19}_{-0.14}$
WR133	HD 190918	WN5o+O9I	$1.85^{+0.16}_{-0.14}$	g	0.36 ± 0.21	0.15 ± 0.09	$0.08^{+0.05}_{-0.05}$
WR113-2	SMG09 1425_47	WC5-6	$1.86^{+0.90}_{-0.56}$	g		0.65 ± 0.21	$0.35^{+0.21}_{-0.16}$
WR70-5	WM10 11b	WC9	$1.95^{+0.75}_{-0.47}$	g		1.26 ± 0.26	$0.65^{+0.28}_{-0.21}$
WR98	HDE 318016	WN8o/C7	$1.96^{+0.31}_{-0.24}$	g	1.59 ± 0.21	0.68 ± 0.09	$0.35^{+0.07}_{-0.06}$
WR25	HD 93162	O2.5If*/WN6+O	$1.97^{+0.18}_{-0.15}$	g	0.62 ± 0.21	0.26 ± 0.09	$0.13^{+0.05}_{-0.05}$
WR135	HD 192103	WC8	$1.98^{+0.18}_{-0.15}$	g	0.41 ± 0.21	0.18 ± 0.09	$0.09^{+0.05}_{-0.05}$
WR85	HD 155603B	WN6h	$1.99^{+0.30}_{-0.24}$	g	1.03 ± 0.21	0.44 ± 0.09	$0.22^{+0.06}_{-0.05}$

distance moduli of the stars and any other helpful information (e.g apparent magnitudes), if their absolute magnitudes could not be calculated.

For all subsequent analysis we use only the most photometrically reliable results, which have a 'b:' or 'g' flag in either the v^{WR} band, or the K_s band. These data do not have high astrometric excess noise ('a') *Gaia* data quality flags. Results with, for example, two 'b' flags were excluded. These flags are applied to the absolute magnitudes in Tables 7 and 6.

We note that 13 objects retained in this selection process had either negative parallax ('n') or high parallax to error ratio ('e') *Gaia* flags. However, the reliable absolute magnitudes mean the distances may still be valid.

4 NEW DISTANCES TO WR STARS AND COMPARISON TO OTHER *Gaia* DERIVED DISTANCES

We can compare the WR star sample from *Gaia* to the total population. There is no substantial difference between the latitude and longitude distribution of WR stars detected in *Gaia* and the total known WR distribution. The exception is for some regions, such as around Westerlund 1 and towards the Galactic Centre, which went undetected by *Gaia* due to their high extinctions (with $A_V > 30$ mag in the latter case).

Crowding presented an additional challenge. WR 43A and 43B are not included in the final distance catalogue as the same *Gaia* source was detected for both stars. The detection for WR43C is also spurious, as the position overlaps with other objects. These stars are located in the compact cluster NGC 3603 (Melena et al. 2008, Crowther & Dessart 1998) and therefore blending is to be expected. It is possible that further stars are missing parallaxes due to crowding,

as this issue would reduce the quality of the *Gaia* five parameter solution below acceptable limits, and cause it to be excluded from the *Gaia* catalogue.

Finally, some stars may not have been detected due to their close binary companions. [Arenou et al. \(2018\)](#) shows that completeness falls for separations below $2''$, to a limit at $0.12''$. This may account for three missing stars with narrowband $v^{\text{WR}} < 15$ mag (WR2, WR63 and WR86), two of which (WR63 and WR86) have known companions.

Table 1 includes distances for each WR star with measured parallaxes. Also included are the 68% credible intervals. Table 8 lists the closest WR stars (with reliable results) within 2 kpc of the Sun. We find 26 WR stars within this distance, similar to the 30 WR stars within 2 kpc from [Conti et al. \(1983\)](#). We also calculate distances to O stars using our Bayesian prior and GOSC v4.1 ([Maíz Apellániz et al. 2013](#)). For the O star population within 2 kpc, we obtain a WR/O ratio of 0.10. This ratio is within the 0.07–0.10 range of [Conti et al. \(1983\)](#), found by comparing lifetimes of H and He core burning phases from massive star models, as an analogue to O star and WR star phases. However, our ratio includes all O stars, and not just the most massive population that WR stars are descended from. [Conti et al. \(1983\)](#) also calculate a WR/O ratio with only O stars $>40M_{\odot}$, and find a much higher ratio of 0.36 ± 0.15 .

Table 8 also includes K_s -band extinctions, and extinctions per kpc for these nearby WR stars, with $A_{K_s}/\text{kpc} \sim 0.28$ mag, albeit with significant star-to-star variation. Dust extinctions of stars in common with the 3D dust map from Pan-STARRS1 and 2MASS [Green et al. \(2015\)](#) shows reasonable overall agreement.

4.1 Comparison with previous WR distances

[Rosslowe & Crowther \(2015a\)](#) provide distance estimates for 228 Galactic WR stars based on previous absolute magnitude calibrations. Of those, 87 have reliable distances from this work. Fig. 13(a) compares distances to Galactic WR stars in common with [Rosslowe & Crowther \(2015a\)](#). Agreement is reasonable up to ~ 2 kpc. This is the subset of *Gaia* sources with the lowest uncertainties and extinction, enabling accurate applications of our prior and absolute magnitude calibrations. Beyond 2 kpc, there is significant scatter, with many stars closer than previously thought. These are principally more highly reddened WR stars that have been discovered recently. Conversely many stars that were thought to be nearby based on calibrations, have significantly larger distances (e.g. WR57 is revised from 2.98 ± 0.52 kpc to $5.50^{+1.49}_{-1.06}$ kpc).

All of our 188 stars with reliable absolute magnitudes have distance estimates from [Bailer-Jones et al. \(2018\)](#). Comparisons are presented in Figure 13(b). Again, good agreement is obtained up to ~ 2 kpc, beyond which the [Bailer-Jones et al. \(2018\)](#) distances are generally larger than our results. The average ω/σ_{ω} for stars at distances beyond 2.5 kpc is -0.71 . The error is therefore a substantial proportion of the total parallax, which suggests disparities stem primarily from limitations in the *Gaia* data and the differences between the two priors. At large distances and so proportionally large parallax errors, the prior dominates the

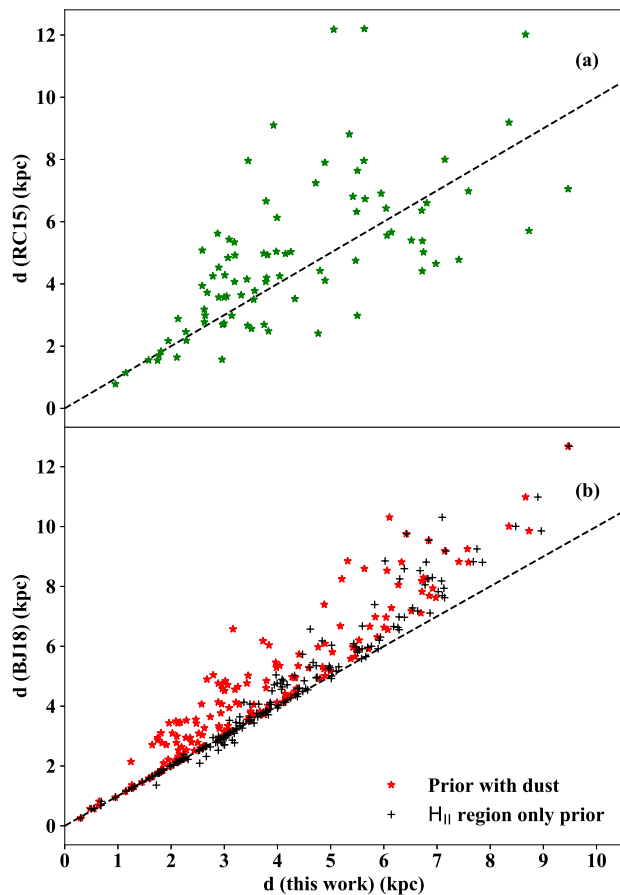


Figure 13. (a) A comparison between distances to Galactic WR stars in common between this work and [Rosslowe & Crowther \(2015a\)](#). The black dashed line indicates one-to-one agreement. Error bars from [Rosslowe & Crowther \(2015a\)](#) have been omitted for clarity; (b) A comparison between WR distances obtained in this work and [Bailer-Jones et al. \(2018\)](#). We illustrate the effect of extinction by presenting the full prior including both dust and HII regions (red stars) and a prior with only HII regions (black cross).

data and the peak of the posterior shifts closer to the peak of the prior.

For this work, the peak of the prior probability defaults to <3 kpc, depending on longitude. If the peak in the Bailer-Jones prior is substantially closer or further, this results in a large divergence between the two measures. Our prior differs significantly from [Bailer-Jones et al. \(2018\)](#) as it more directly accounts for extinction and the specific distribution of massive stars. The red stars/black crosses in Figure 13(b) show the contrast between results calculated with/without the dust extinction model. In most instances, the stars had results more in line with [Bailer-Jones et al. \(2018\)](#) when dust was excluded. Therefore, in the vast majority of cases, dust extinction in the prior is the primary factor leading to different results.

Since distances from [Bailer-Jones et al. \(2018\)](#) formed the basis of the recent spectroscopic studies of Galactic WR stars by [Sander et al. \(2019\)](#) and [Hamann et al. \(2019\)](#), use of distances from this study with no warning flags would lead to generally modest 0.05 dex reductions in stellar luminosity.

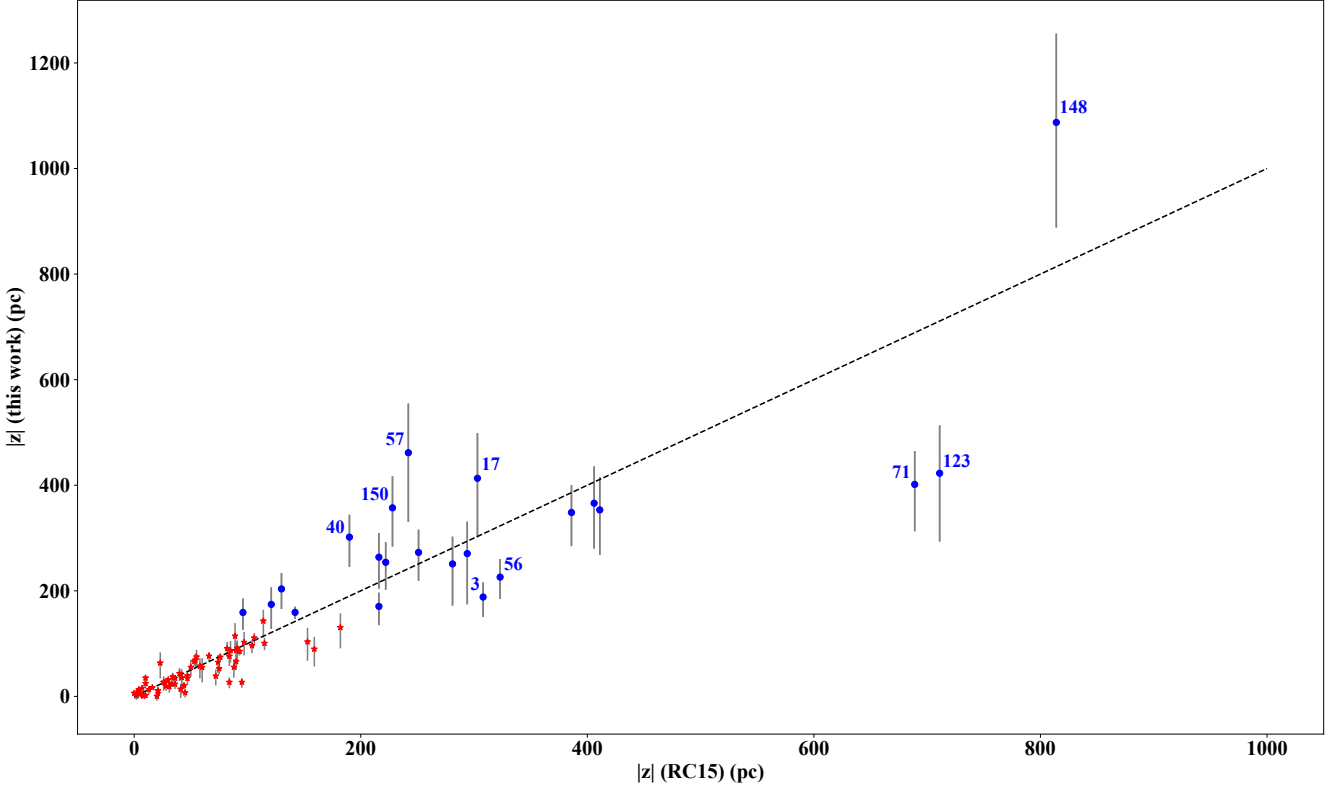


Figure 14. A comparison between the WR distances from the midplane from [Rosslowe & Crowther \(2015a\)](#) and this work. Blue circles are the points from this work with distances greater than 3σ , where σ is the HII region scale height. The dotted line indicates parity between the two measures. Stars with significant disagreement are labelled with their WR numbers.

These are included in Table 1, with higher reductions for relatively distant stars including WR74 (WN7o, 0.24 dex), WR91 (WN7b, 0.23 dex), WR56 (WC7, 0.20 dex) and WR64 (WC7, 0.20 dex).

We also compare the distances to a Galactic LBV (WR31b = AG Car) and LBV candidate (WR31a = He 3-519) which are in common with [Smith et al. \(2019\)](#). They obtain a distance of $7.12^{+2.53}_{-1.67}$ kpc to WR31a, versus $7.35^{+1.45}_{-1.18}$ kpc from this work, and $4.65^{+1.43}_{-0.92}$ kpc to WR31b, versus $4.85^{+0.93}_{-0.70}$ kpc from this work. These are well within the uncertainties of both stars, particularly given WR31a has a high error to parallax ratio of 0.72 (as measured directly from the catalogue values). [Smith et al. \(2019\)](#) adopt a different zero point to our study, namely 0.05 mas as an initial value and modelling some uncertainty in this as part of their calculation. This decision is based on the variety of different zero points found in the literature (e.g. [Riess et al. 2018](#), [Zinn et al. 2019](#), [Stassun & Torres 2018](#) and [Graczyk et al. 2019](#)).

Therefore, these distances are systematically closer than those from [Bailer-Jones et al. \(2018\)](#). This result agrees both with our findings and [Schönrich et al. \(2019\)](#), who also find that [Bailer-Jones et al. \(2018\)](#) appear to systematically overestimate distances. As [Smith et al. \(2019\)](#) adopts a similar prior to that of [Bailer-Jones et al. \(2018\)](#), the overlapping results therefore indicate that the larger zero point is performing much the same function as our dust model, acting to moderate the distances of [Bailer-Jones et al. \(2018\)](#).

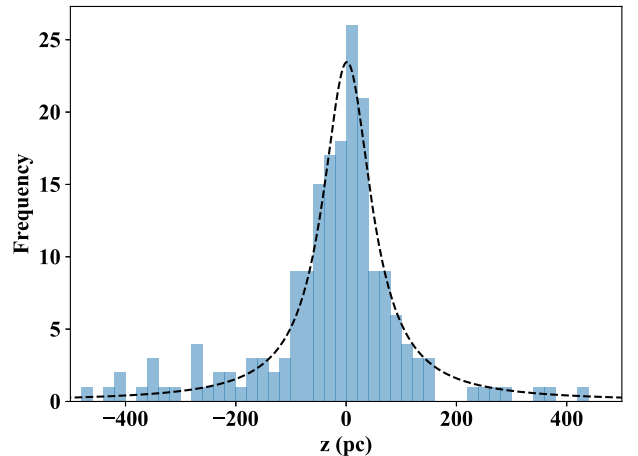


Figure 15. A histogram distribution of WR distances from the Galactic disk. The dotted line shows the Cauchy fit from Equation 3.

5 DISTANCES FROM THE GALACTIC DISK

To identify potential runaway stars, we calculated distances from the Galactic plane using the most likely distance from the Sun and the Galactic latitude of the star, with the addition of the 20.8 pc ([Bennett & Bovy 2019](#)) for the Sun's distance above the midplane. The 68% distance uncertainty intervals were scaled to give height uncertainties.

The new midplane distances in Table 1 are compared with results from [Rosslowe & Crowther \(2015a\)](#) in Figure 14. In general, the deviation from previous results increases with height, reflecting the uncertainty of distances to very remote WR stars. The scale heights, σ , of HII regions loosely trace massive star formation sites and can therefore highlight potential runaways. Based on the median north scale height between 3.9 kpc and 5.6 kpc in [Paladini et al. \(2004\)](#), σ is 52 pc. The south scale heights contained too few points to be reliable.

We additionally calculated the scale height of the WR population. The histogram of WR distances from the midplane is presented in Figure 15 and can be fit with a Cauchy distribution

$$g = \frac{A}{\pi\gamma} \frac{\gamma^2}{(z-c)^2 + \gamma^2} \quad (3)$$

where A is the scale constant, c is the distribution centre and γ is the scale parameter, specifying the half width half maximum (HWHM). Fitting these parameters gives a centre of 1.5 pc and a HWHM of 53.7 pc. The central value of our distribution is similar to [Rosslowe & Crowther \(2015a\)](#) (1.9 pc), though the HWHM is somewhat smaller, at 39.2 pc. The central value would suggest many WR stars are slightly above the plane, but this may be due to planar dust extinction rendering WR stars which sit below the disk being inaccessible to *Gaia*.

Our results are similar to [Conti & Vacca \(1990\)](#), who find a WR scale height of 45 ± 5 pc using an isothermal disk model and [Bobylev & Bajkova \(2016\)](#), who obtained a height 51.3 ± 3.7 pc using the same method. However, this latter value relies on a sample at < 4 kpc (excluding distant stars to avoid the effects of Galactic disk warp) and thus only covers about half the WR stars in our sample.

To identify only the most extreme runaways and ensure they did not form in situ, we apply a 3σ cut-off using the HII region scale height. Since a velocity of 1 km s^{-1} equates to 1 pc Myr^{-1} , runaways ($\geq 30 \text{ km s}^{-1}$) will travel in excess of 150 pc over a typical WR lifetime of 5 Myr. 91% of 383 WR stars in *Gaia* reside within three scale heights from the Galactic plane, so 9 % of WR stars are located far from the Galactic plane. Table 9 presents the $|z|$ distances for each of these stars.

However, the resulting runaway list does not account for the known warp in the Galactic disk. [Romero-Gómez et al. \(2019\)](#) estimate the warp begins at a radius of 12-13 kpc from the Galactic centre for their sample of young, bright stars (which they refer to as the OB sample). All but two of our WR stars are within 12 kpc of the Galactic centre and by this measure, would be unaffected. However, their results show some complex structures that in fact suggest some of our sample may be affected by the warp. An alternative measure from [Li et al. \(2019\)](#), estimates that the Galactic disk instead begins to warp at a radius of 9.2 kpc. 20 stars are further from the centre than this distance, and so their heights would need to account for the warp.

To obtain a robust candidate list of runaways with $\geq 30 \text{ km s}^{-1}$, we used the Galactic warp model and onset from [Li et al. \(2019\)](#) to calculate the height of the Galactic plane at the position of each of the 383 WR stars with distances. We subtracted off the height of this Galactic warp, which produced a distance from the midplane for each star, which

accounted for the warp. These distances were then used to exclude any stars which were not 3σ from the plane, once the warp was accounted for. Using this method, we excluded WR8 and WR12 from our runaway list in Table 9. Therefore, 31 stars (8 % of WR stars in *Gaia*) are robust runaway candidates.

We do not apply the warp to our full list of distances from the plane in Table 1, as the warp onset and model are still uncertain.

The runaways identified in [Rosslowe & Crowther \(2015a\)](#) generally remain far from the plane. However, many of the more extreme distances from the plane are now moderated, due to reduced distances from the Sun. This suggests that extreme runaways are less common than previously thought. WR93a and WR64 are not included, as they were identified as having abnormal v^{WR} band extinction (Section 3), which meant it was not possible to calculate their absolute magnitudes, so their distances could not be validated.

Two main evolutionary paths may have created these runaways. The first is the disruption of a binary system when the primary star explodes as a supernova and ejects the remaining companion ([Blaauw 1961](#)). The second scenario is dynamical ejection from a dense cluster, which can eject both binary and single stars ([Poveda et al. 1967](#)). The majority of outliers with $> 3\sigma$ distances are apparently single stars, as only WR30 and WR69 have confirmed OB companions.

As both single stars and binaries can be ejected from clusters, it is not possible for us to definitively state which mechanism is dominant. We defer a discussion of the origin of runaways to Paper II which considers the association of WR stars with star clusters or OB associations. However, we note that recent simulations suggest fast runaways from either mechanism are anticipated to be very rare ([Renzo et al. 2019](#); [Oh & Kroupa 2016](#)), in stark contrast with the high fraction of WR stars at extreme distances from the Galactic plane.

Two stars merit individual consideration. The high velocity runaway WR124 is now located at $|z|=360$ pc, compared to previous estimates of 217 pc ([Rosslowe & Crowther 2015a](#)), 193 pc ([Marchenko et al. 2010](#)) and 250 pc ([Moffat et al. 1982](#)). This confirms its runaway status, although our work places it significantly further from the Sun (5.9 kpc instead of 3.3 kpc from [Marchenko et al. 2010](#)).

WR148 is located furthest from the Galactic plane. [Drissen et al. \(1986\)](#) suggested it as a possible WR+compact object binary disrupted by a SN, however, [Munoz et al. \(2017\)](#) claim it is instead a WN+O binary. If the latter is true, our data suggests that WR148 is a binary system that has been ejected from a cluster, concurring with [Munoz et al. \(2017\)](#). Assuming a lifetime of 5 Myr and a straight vertical trajectory from the Galactic disk, the minimum possible velocity for WR148 is 212 km s^{-1} , making it a very rapid cluster ejection.

[Moffat \(1989\)](#) suggested WN8-9 were over represented amongst runaways, a finding which was corroborated by [Rosslowe & Crowther \(2015a\)](#). However amongst our sample, only 4 out of 31 stars are of the WN8-9 subtype. The previous over representation disappears with the drop in extreme runaways. If our sample is representative of the wider WR star population, this suggests that the observed dis-

Table 9. Distance of WR stars from the midplane $|z|$, for which excesses exceed 3σ , where $\sigma=52$ pc, the HII region scale height of 52 pc. Previously identified runaways with $|z| \geq 300$ pc according to Rosslowe & Crowther (2015a) are also indicated

WR Number	Spectral type	Dist (kpc)	$ z $ (pc)	HII σ	Known runaway
WR148	WN8h+	$9.47^{+1.77}_{-1.49}$	1087^{+199}_{-168}	$20.9^{+3.8}_{-3.2}$	Yes
WR57	WC8	$5.50^{+1.49}_{-1.06}$	462^{+131}_{-93}	$8.9^{+2.5}_{-1.8}$	No
WR123	WN8o	$5.35^{+1.56}_{-1.09}$	423^{+129}_{-91}	$8.1^{+2.5}_{-1.7}$	Yes
WR73	WC9d	$6.81^{+1.85}_{-1.47}$	423^{+109}_{-87}	$8.1^{+2.1}_{-1.7}$	No
WR17	WC5	$6.75^{+1.74}_{-1.33}$	413^{+112}_{-86}	$7.9^{+2.1}_{-1.6}$	Yes
WR71	WN6o	$3.19^{+0.67}_{-0.48}$	402^{+89}_{-63}	$7.7^{+1.7}_{-1.2}$	Yes
WR6	WN4b	$2.27^{+0.42}_{-0.31}$	376^{+73}_{-54}	$7.2^{+1.4}_{-1.0}$	No
WR75c	WC9	$7.15^{+1.78}_{-1.45}$	366^{+86}_{-70}	$7.0^{+1.7}_{-1.3}$	Yes
WR124	WN8h	$5.87^{+1.48}_{-1.09}$	360^{+85}_{-63}	$6.9^{+1.6}_{-1.2}$	Yes
WR150	WC5	$8.73^{+1.70}_{-1.38}$	357^{+73}_{-60}	$6.9^{+1.4}_{-1.1}$	No
WR61	WN5o	$5.49^{+1.25}_{-0.91}$	353^{+85}_{-62}	$6.8^{+1.6}_{-1.2}$	Yes
WR49	WN5(h)	$8.35^{+1.44}_{-1.17}$	348^{+64}_{-52}	$6.7^{+1.2}_{-1.0}$	Yes
WR58	WN4b/CE	$5.88^{+1.42}_{-1.04}$	337^{+86}_{-63}	$6.5^{+1.7}_{-1.2}$	No
WR40	WN8h	$3.83^{+0.67}_{-0.50}$	302^{+56}_{-42}	$5.8^{+1.1}_{-0.8}$	No
WR126	WC5/WN	$7.57^{+1.49}_{-1.19}$	300^{+55}_{-44}	$5.8^{+1.1}_{-0.8}$	No
WR103	WC9d+?	$3.46^{+1.28}_{-0.77}$	275^{+109}_{-65}	$5.3^{+2.1}_{-1.3}$	No
WR33	WC5; WC6	$7.59^{+1.62}_{-1.30}$	273^{+54}_{-43}	$5.2^{+1.0}_{-0.8}$	No
WR69	WC9d+OB	$3.48^{+0.64}_{-0.47}$	272^{+54}_{-40}	$5.2^{+1.0}_{-0.8}$	No
WR92	WC9	$3.78^{+1.25}_{-0.79}$	271^{+96}_{-61}	$5.2^{+1.8}_{-1.2}$	No
WR54	WN5o	$6.52^{+1.37}_{-1.05}$	264^{+60}_{-46}	$5.1^{+1.1}_{-0.9}$	Yes
WR129	WN4o	$5.47^{+1.22}_{-0.90}$	254^{+52}_{-38}	$4.9^{+1.0}_{-0.7}$	No
WR83	WN5o	$3.80^{+1.10}_{-0.72}$	251^{+79}_{-52}	$4.8^{+1.5}_{-1.0}$	No
WR131	WN7h+abs	$6.92^{+1.40}_{-1.09}$	227^{+42}_{-32}	$4.4^{+0.8}_{-0.6}$	No
WR56	WC7	$8.67^{+1.46}_{-1.20}$	226^{+41}_{-34}	$4.3^{+0.8}_{-0.7}$	Yes
WR30	WC6+O6-8	$5.09^{+0.99}_{-0.74}$	211^{+45}_{-33}	$4.1^{+0.9}_{-0.6}$	No
WR20	WN5o	$6.98^{+1.18}_{-0.93}$	204^{+38}_{-30}	$3.9^{+0.7}_{-0.6}$	No
WR3	WN3ha	$2.90^{+0.52}_{-0.39}$	188^{+38}_{-28}	$3.6^{+0.7}_{-0.5}$	Yes
WR4	WC5+?	$3.75^{+0.89}_{-0.62}$	174^{+47}_{-32}	$3.4^{+0.9}_{-0.6}$	No
WR128	WN4(h)	$2.90^{+0.54}_{-0.39}$	170^{+35}_{-26}	$3.3^{+0.7}_{-0.5}$	No
WR52	WC4	$1.75^{+0.16}_{-0.13}$	159^{+13}_{-11}	$3.1^{+0.2}_{-0.2}$	No
WR34	WN5o	$7.41^{+1.37}_{-1.09}$	159^{+33}_{-26}	$3.1^{+0.6}_{-0.5}$	No

tribution was due to overestimated distance measurements, which would have made the stars appear further from the plane than they truly are.

6 CONCLUSIONS

We have calculated distances and absolute magnitudes of the Galactic WR population using data from *Gaia* DR2:

- 383 WR stars (58% of the known Galactic population) have full five parameter astrometric solutions (proper motions and parallaxes) in the *Gaia* catalogue. WR stars with large J–K>3 colours, indicating high dust extinctions, were generally not detected by *Gaia*.
- We used the *Gaia* parallaxes to calculate distances to the 383 WR stars detected by *Gaia*. We use Bayesian methods to properly transform the parallax uncertainties to distance uncertainties and to obtain distances from negative parallaxes. Our Bayesian prior accounts for extinction using a Galactic dust model and the specific distribution of massive stars using HII regions. Potential underestimates of parallax uncertainties and the zero point error are accounted for in our calculation.
- The resulting distances agree well with both the previous calibration (Rosslowe & Crowther 2015a) and DR2 distances from Bailer-Jones et al. (2018) up to 2 kpc. Deviations above 2 kpc are due primarily to the large uncertainties of the *Gaia* parallaxes. Distances from Bailer-Jones et al. (2018) formed the basis of recent spectroscopic studies of Galactic WR stars by Sander et al. (2019) and Hamann et al. (2019). Use of distances from this study would generally lead to modest 0.05 dex reductions in stellar luminosities, albeit with reductions of up to 0.2 dex for relatively distant stars.
- 26 WR stars are found within 2 kpc, compared to 30 WR stars from Conti et al. (1983). Based on the population in GOSC v4.1 (Maíz Apellániz et al. 2013), the WR/O star ratio in this region is 0.10.
- We calculate absolute magnitudes for WR stars, in both the v^{WR} and K_s bands. Of these, 188 stars have an absolute magnitude in either band and were used to generate subtype averages for calibrations. Both WN and WC stars are found to be more diverse in their absolute magnitude ranges than anticipated and therefore we recommend avoiding use of calibrations without accounting for this large intrinsic spread.
- We have applied our new distances to identify 31 potential runaways from the Galactic disk, accounting for the Galactic warp. HII region scale heights define the cut-offs for runaway status. 20 of these WR stars with $|z|>156$ pc are new detections. The vast majority of the runaway stars are single. However, as both companion supernovae and dynamical ejection from clusters can produce single star runaways, it was not possible for us to determine the dominant runaway production mechanism, which is deferred to Paper II.

The current limitations of our prior are mainly the simplified dust extinction map. With an increased number of observations, the quality of future *Gaia* release data should improve. Therefore, the number of WR stars with negative parallaxes should fall and we thus expect a corresponding decrease in the number of flagged results. Better parallax to error ratios in the early DR3 release (estimated to improve by a factor 1.2, Brown 2019), will also reduce uncertainties and the effect of our prior when used with small parallaxes. Further improvements to the astrometric modelling and fitting algorithms should also reduce the number of questionable results via a reduction in astrometric excess noise. Finally, there is a possibility that the number of WR stars with distances will increase. 32 objects only had two pa-

parameter solutions (fitting positions) from *Gaia* DR2. Future *Gaia* data releases may find satisfactory full five parameter solutions, which would also include parallaxes.

ACKNOWLEDGEMENTS

GR wishes to thank the Science and Technology Facilities Council (STFC), for their financial support through the Doctoral Training Partnership.

We wish to thank the referee Dr Anthony Brown for his helpful comments and suggestions on the submitted manuscript. We also thank Josep Manel Carrasco and Carme Jordi for providing the synthetic photometry in V broadband, *Gaia* $G_{BP} - G_{RP}$ and G filters at different extinctions and for different WR star subtypes, used in Section 3.3.

This work has made use of data from the European Space Agency (ESA) mission *Gaia* (<https://www.cosmos.esa.int/gaia>), processed by the *Gaia* Data Processing and Analysis Consortium (DPAC, <https://www.cosmos.esa.int/web/gaia/dpac/consortium>). Funding for the DPAC has been provided by national institutions, in particular the institutions participating in the *Gaia* Multilateral Agreement.

This publication also makes use of data products from the Two Micron All Sky Survey, which is a joint project of the University of Massachusetts and the Infrared Processing and Analysis Center/California Institute of Technology, funded by the National Aeronautics and Space Administration and the National Science Foundation.

The work in Section 2.1 is based on data products from observations made with ESO Telescopes at the La Silla Paranal Observatory under programme ID 177.D-3023, as part of the VST Photometric $H\alpha$ Survey of the Southern Galactic Plane and Bulge (VPHAS+, www.vphas.eu). Additionally, this paper makes use of data obtained as part of the INT Photometric $H\alpha$ Survey of the Northern Galactic Plane (IPHAS, www.iphas.org) carried out at the Isaac Newton Telescope (INT). The INT is operated on the island of La Palma by the Isaac Newton Group in the Spanish Observatorio del Roque de los Muchachos of the Instituto de Astrofísica de Canarias. All IPHAS data are processed by the Cambridge Astronomical Survey Unit, at the Institute of Astronomy in Cambridge. The bandmerged DR2 catalogue was assembled at the Centre for Astrophysics Research, University of Hertfordshire, supported by STFC grant ST/J001333/1.

In addition to Astropy ([Astropy Collaboration et al. 2013](#)), this work would not be possible without the python packages Numpy ([Oliphant 2006](#), [Walt et al. 2011](#)), Pandas ([McKinney 2010](#)) and Matplotlib ([Hunter 2007](#)).

REFERENCES

- Arenou F., et al., 2018, *A&A*, **616**, A17
- Astropy Collaboration et al., 2013, *A&A*, **558**, A33
- Astropy Collaboration et al., 2018, *AJ*, **156**, 123
- Bailer-Jones C. A. L., 2015, *Publications of the Astronomical Society of the Pacific*, **127**, 994
- Bailer-Jones C. A. L., Rybizki J., Fouesneau M., Mantelet G., Andrae R., 2018, *AJ*, **156**, 58
- Barentsen G., et al., 2014, *MNRAS*, **444**, 3230
- Bennett M., Bovy J., 2019, *MNRAS*, **482**, 1417
- Bessell M. S., 1979, *Publications of the Astronomical Society of the Pacific*, **91**, 589
- Blaauw A., 1961, *Bulletin of the Astronomical Institutes of the Netherlands*, **15**, 265
- Bobylev V. V., Bajkova A. T., 2016, *Astronomy Letters*, **42**, 1
- Brown A. G., 2019, The Future of the Gaia Universe, doi:10.5281/zenodo.2637972, <https://doi.org/10.5281/zenodo.2637972>
- Cardelli J. A., Clayton G. C., Mathis J. S., 1989, *ApJ*, **345**, 245
- Chené A. N., et al., 2019, *MNRAS*, **484**, 5834
- Cohen M., van der Hucht K. A., Williams P. M., The P. S., 1991, *ApJ*, **378**, 302
- Conti P. S., Massey P., 1989, *ApJ*, **337**, 251
- Conti P. S., Vacca W. D., 1990, *AJ*, **100**, 431
- Conti P. S., Garmany C. D., De Loore C., Vanbeveren D., 1983, *ApJ*, **274**, 302
- Crowther P. A., 2007, *ARAA*, **45**, 177
- Crowther P. A., Dessart L., 1998, *MNRAS*, **296**, 622
- Crowther P. A., Smith L. J., 1997, *A&A*, **320**, 500
- Crowther P. A., Smith L. J., Hillier D. J., Schmutz W., 1995, *A&A*, **293**, 427
- Crowther P. A., Dessart L., Hillier D. J., Abbott J. B., Fullerton A. W., 2002, *A&A*, **392**, 653
- Crowther P. A., Hadfield L. J., Clark J. S., Negueruela I., Vacca W. D., 2006, *MNRAS*, **372**, 1407
- De Marco O., Schmutz W., Crowther P. A., Hillier D. J., Dessart L., de Koter A., Schweickhardt J., 2000, *A&A*, **358**, 187
- Drew J. E., et al., 2005, *MNRAS*, **362**, 753
- Drew J. E., et al., 2014, *MNRAS*, **440**, 2036
- Drissen L., Lamontagne R., Moffat A. F. J., Bastien P., Seguin M., 1986, *ApJ*, **304**, 188
- Ducati J. R., Bevilacqua C. M., Rembold S. r. B., Ribeiro D., 2001, *ApJ*, **558**, 309
- Eldridge J. J., Fraser M., Smartt S. J., Maund J. R., Crockett R. M., 2013, *MNRAS*, **436**, 774
- Evans D. W., et al., 2018, *A&A*, **616**, A4
- Fritz T. K., et al., 2011, *ApJ*, **737**, 73
- Gaia Collaboration et al., 2016, *A&A*, **595**, A1
- Gaia Collaboration et al., 2018a, *A&A*, **616**, A1
- Gaia Collaboration et al., 2018b, *A&A*, **616**, A10
- Geogy C., Meynet G., Walder R., Folini D., Maeder A., 2009, *A&A*, **502**, 611
- Götberg Y., de Mink S. E., Groh J. H., Kupfer T., Crowther P. A., Zapartas E., Renzo M., 2018, *A&A*, **615**, A78
- Graczyk D., et al., 2019, *ApJ*, **872**, 85
- Gravity Collaboration et al., 2018, *A&A*, **615**, L15
- Green G. M., et al., 2015, *ApJ*, **810**, 25
- Hadfield L. J., van Dyk S. D., Morris P. W., Smith J. D., Marston A. P., Peterson D. E., 2007, *MNRAS*, **376**, 248
- Hainich R., et al., 2014, *A&A*, **565**, A27
- Hamann W.-R., Gräfener G., 2004, *A&A*, **427**, 697
- Hamann W. R., Gräfener G., Liermann A., 2006, *A&A*, **457**, 1015
- Hamann W. R., et al., 2019, *A&A*, **625**, A57
- Hambly N., et al., 2018, Technical report, Gaia DR2 documentation Chapter 14: Datamodel description
- Hogg D. W., 2018, preprint, p. [arXiv:1804.07766](https://arxiv.org/abs/1804.07766) ([arXiv:1804.07766](https://arxiv.org/abs/1804.07766))
- Hunter J. D., 2007, *Computing in Science and Engineering*, **9**, 90
- Jordi C., et al., 2010, *A&A*, **523**, A48
- Kippenhahn R., Weigert A., 1967, *zap*, **65**, 251
- Leloudas G., Sollerman J., Levan A. J., Fynbo J. P. U., Malesani D., Maund J. R., 2010, *aap*, **518**, A29
- Li C., Zhao G., Jia Y., Liao S., Yang C., Wang Q., 2019, *ApJ*, **871**, 208
- Lindgren L., et al., 2018a, Gaia DR2 astrometry, <https://www.cosmos.esa.int/web/gaia/dr2-known-issues>
- Lindgren L., et al., 2018b, *A&A*, **616**, A2
- Lundström I., Stenholm B., 1984, *Astronomy and Astrophysics Supplement Series*, **58**, 163
- Luri X., et al., 2018, *A&A*, **616**, A9
- Maíz Apellániz J., Weiler M., 2018, *A&A*, **619**, A180
- Maíz Apellániz J., et al., 2013, in *Massive Stars: From alpha to Omega*. p. 198 ([arXiv:1306.6417](https://arxiv.org/abs/1306.6417))
- Marchenko S. V., Moffat A. F. J., Crowther P. A., 2010, *ApJ*, **724**, L90
- Martins F., Plez B., 2006, *A&A*, **457**, 637
- Mason B. D., Hartkopf W. I., Gies D. R., Henry T. J., Helsel J. W., 2009, *AJ*, **137**, 3358
- Mauerhan J. C., Van Dyk S. D., Morris P. W., 2009, *PASP*, **121**, 591
- McKinney W., 2010, in van der Walt S., Millman J., eds, *Proceedings of the 9th Python in Science Conference*. pp 51 – 56
- Melena N. W., Massey P., Morrell N. I., Zangari A. M., 2008, *AJ*, **135**, 878
- Meynet G., Maeder A., 2005, *A&A*, **429**, 581
- Moffat A. F. J., 1989, *ApJ*, **347**, 373
- Moffat A. F. J., Lamontagne R., Seggewiss W., 1982, *A&A*, **114**, 135

- Munoz M., Moffat A. F. J., Hill G. M., Shenar T., Richardson N. D., Pablo H., St-Louis N., Ramiamanantsoa T., 2017, *MNRAS*, **467**, 3105
- Oh S., Kroupa P., 2016, *A&A*, **590**, A107
- Oliphant T., 2006, Guide to NumPy
- Paladini R., Burigana C., Davies R. D., Maino D., Bersanelli M., Cappellini B., Platania P., Smoot G., 2002, VizieR Online Data Catalog, pp J/A+A/397/213
- Paladini R., Burigana C., Davies R. D., Maino D., Bersanelli M., Cappellini B., Platania P., Smoot G., 2003, *A&A*, **397**, 213
- Paladini R., Davies R. D., De Zotti G., 2004, *MNRAS*, **347**, 237
- Poveda A., Ruiz J., Allen C., 1967, Boletín de los Observatorios Tonantzintla y Tacubaya, **4**, 86
- Renzo M., et al., 2019, *A&A*, **624**, A66
- Riess A. G., et al., 2018, *ApJ*, **861**, 126
- Romero-Gómez M., Mateu C., Aguilar L., Figueras F., Castro-Ginard A., 2019, *A&A*, **627**, A150
- Rosslove C. K., Crowther P. A., 2015a, *MNRAS*, **447**, 2322
- Rosslove C. K., Crowther P. A., 2015b, *MNRAS*, **449**, 2436
- Salgado J., González-Núñez J., Gutiérrez-Sánchez R., Segovia J. C., Durán J., Hernández J. L., Arviset C., 2017, *Astronomy and Computing*, **21**, 22
- Sana H., et al., 2012, *Science*, **337**, 444
- Sander A., Hamann W. R., Todt H., 2012, *A&A*, **540**, A144
- Sander A. A. C., Hamann W. R., Todt H., Hainich R., Shenar T., Ramachandran V., Oskinova L. M., 2019, *A&A*, **621**, A92
- Schnurr O., Moffat A. F. J., St-Louis N., Morrell N. I., Guerrero M. A., 2008, *MNRAS*, **389**, 806
- Schönrich R., McMillan P., Eyer L., 2019, *MNRAS*, **487**, 3568
- Shara M. M., et al., 2009, *AJ*, **138**, 402
- Shenar T., et al., 2019, *A&A*, **627**, A151
- Skrutskie M. F., et al., 2006, *AJ*, **131**, 1163
- Smith L. F., 1968, *MNRAS*, **140**, 409
- Smith L. F., Shara M. M., Moffat A. F. J., 1990, *ApJ*, **358**, 229
- Smith L. J., Crowther P. A., Prinja R. K., 1994, *A&A*, **281**, 833
- Smith L. F., Shara M. M., Moffat A. F. J., 1996, *MNRAS*, **281**, 163
- Smith N., Li W., Filippenko A. V., Chornock R., 2011, *Monthly Notices of the Royal Astronomical Society*, **412**, 1522
- Smith N., Aghakhanloo M., Murphy J. W., Drout M. R., Stassun K. G., Groh J. H., 2019, *MNRAS*, **488**, 1760
- Stassun K. G., Torres G., 2018, *ApJ*, **862**, 61
- Stead J. J., Hoare M. G., 2009, *MNRAS*, **400**, 731
- Todt H., Sander A., Hainich R., Hamann W.-R., Quade M., Shenar T., 2015, *A&A*, **579**, A75
- Torres-Dodgen A. V., Massey P., 1988, *AJ*, **96**, 1076
- Torres A. V., Conti P. S., Massey P., 1986, *ApJ*, **300**, 379
- Tramper F., et al., 2015, *A&A*, **581**, A110
- Turner D. G., 1982, in *Wolf-Rayet Stars: Observations, Physics, Evolution*. pp 57–60
- Vacca W. D., Torres-Dodgen A. V., 1990, *ApJS*, **73**, 685
- Walt S. v. d., Colbert S. C., Varoquaux G., 2011, *Computing in Science & Engineering*, **13**, 22
- Wenger M., et al., 2000, *Astronomy and Astrophysics Supplement Series*, **143**, 9
- Williams P. M., van der Hucht K. A., 2000, *MNRAS*, **314**, 23
- Zhekov S. A., Tomov T., Gawronski M. P., Georgiev L. N., Borissova J., Kurtev R., Gagné M., Hajduk M., 2014, *MNRAS*, **445**, 1663
- Zinn J. C., Pinsonneault M. H., Huber D., Stello D., 2019, *ApJ*, **878**, 136
- van Leeuwen F., 2007, *A&A*, **474**, 653
- van der Hucht K. A., 2001, *New Astronomy Reviews*, **45**, 135